Generation and Detection of Lamb Waves for the Characterization of Plastic Deformation

A Thesis
Presented to
The Academic Faculty

by

Christoph Prüll

In Partial Fulfillment
of the Requirements for the Degree
Master of Science in Engineering Science and Mechanics

School of Civil and Environmental Engineering
Georgia Institute of Technology
December 2007

Generation and Detection of Lamb Waves for the Characterization of Plastic Deformation

Approved by:

Dr. Laurence J. Jacobs, Advisor
School of Civil and Environmental Engineering
Georgia Institute of Technology

Dr. Jin–Yeon Kim
School of Civil and Environmental Engineering
Georgia Institute of Technology

Dr. Jianmin Qu
George W. Woodruff School of Mechanical Engineering
Georgia Institute of Technology

Date Approved: August 21, 2007

ACKNOWLEDGEMENTS

I will say thanks to all who made my stay here in Atlanta possible and supported me in this great time during my study at Georgia Institute of Technology in Atlanta.
First, I would like to thank my adviser Prof. Laurence J. Jacobs for his guidance and the good working atmosphere in the office. He also supported me financially so I could present my result of my research on the Quantitative Nondestructive Evaluation (QNDE) conference in Denver, Colorado. Next I also want to thank Dr. Jin–Yeon Kim for his very helpful advise when I became stuck in my experiments. The valuable discussions with him helped me considerably to find the right direction. Many thanks to Kritsakorn Luangvilai for the help, when I had difficulties with the experimental measurements. I thank Prof. Jianmin Qu for his support and the granting of access to the facilities of the School of Mechanical Engineering. For friendship and a good working environment, I express my gratitude to my office co-workers Sebastian Küchler and Richard Kmack.
Additionally, I acknowledge the support of the people and organizations of my home country Germany, including the Institute of Applied and Experimental Mechanics with Prof. Dr.–Ing. Lothar Gaul as head of the ISAP Exchange Program. Also thanks to Dipl.–Ing. Helge Kuttig, who did a great deal of organizational work for us students in the ISAP Exchange Program. The German Academic Exchange Service (DAAD) and state support for studying (BAföG) funded me during the stay in the United States, which enabled my stay on the Georgia Institute of Technology. Last, my gratitude is expressed toward my parents, who supported me throughout my academic carrier especially this year of my study abroad. They had a lot of organizational work to do for me, which I highly recognize.

TABLE OF CONTENTS

ACKNOWLEDGEMENTS . . . . . **iii**

LIST OF TABLES . . . . . **vi**

LIST OF FIGURES . . . . . **vii**

SUMMARY . . . . . **x**

I INTRODUCTION **1**

II FUNDAMENTAL THEORY **4**

2.1 Linear wave propagation 4

2.1.1 Equations of motion 4

2.1.2 Wave phenomena 7

2.1.3 Wave reflection on a plane interface 8

2.1.4 Lamb waves 9

2.2 Nonlinear wave propagation 14

2.3 Nonlinearity parameter β 15

III EXCITATION OF CUMULATIVE SECOND HARMONICS IN LAMB WAVES **20**

3.1 Theoretical fundamentals for cumulative second harmonic 20

3.2 Existence condition for the cumulative second harmonic field 27

IV EXPERIMENTAL PROCEDURE **30**

4.1 Experimental setup 30

4.2 Generation of Lamb waves in wave guides 32

4.2.1 Wedge method 32

4.2.2 Wedge design 34

4.3 Wave detection instrumentation 38

4.3.1 Single probe heterodyne laser interferometer 38

4.3.2 Wedge method 40

4.3.3 Comparison of the laser interferometer and the wedge–transducer method 41

4.4 Specimens 43

4.5 Signal processing 44

V EXPERIMENTAL RESULTS 49

5.1 Evaluation of the system setup and signal processing 49

5.2 The impact of the short–time Fourier transformation window length 51

5.3 Assessment of material nonlinearity change due to plastic deformation 56

5.4 Analysis of the detected signal with a wide short–time Fourier transformation window 58

5.5 Analysis of the detected signal with a narrow short–time Fourier transformation window 63

VI CONCLUSIONS AND FURTHER WORK 69

APPENDIX A — LIMITATION OF THE SHORT–TIME FOURIER TRANSFORMATION RESOLUTION DUE TO THE HEISENBERG UNCERTAINTY 72

REFERENCES 77

LIST OF TABLES

Table 2.1 Angle relations for reflection on a stress–free surface. 9

Table 5.1 Data tables for the different stress and strain level of the specimens. 57

LIST OF FIGURES

Figure 2.1 Momentum balance. 4

Figure 2.2 Wave reflections. (a) Reflection of a P–wave. (b) Reflection of a SV–wave. 9

Figure 2.3 Multiple reflections in a waveguide. 10

Figure 2.4 In–plane (solid line) and out–of–plane (dotted line) displacement distribution for a aluminum plate normalized with wave number k=5. 12

Figure 2.5 Theoretical solution in the phase velocity – frequency domain (dispersion curves). 13

Figure 2.6 Theoretical solution for the Lamb wave. 13

Figure 2.7 Linear and nonlinear wave propagation in a solid. 14

Figure 3.1 Cumulative second harmonic excitation setpoint s1 → s2. 29

Figure 3.2 Mode–curves in time–frequency domain 29

Figure 4.1 Experimental setup. 30

Figure 4.2 Generation of a Lamb wave with the wedge method. 32

Figure 4.3 Snell's law for angle beam analysis. 33

Figure 4.4 Propagation distance in the wedge 35

Figure 4.5 Old wedge design 36

Figure 4.6 Improved wedge design 36

Figure 4.7 Amplitude of the fundamental wave 38

Figure 4.8 Laser interferometer detection system. 39

Figure 4.9 Wave detection with wedge-transducer combination 40

Figure 4.10 Fundamental and second harmonic frequency as functions of time detected with the laser interferometer. 42

Figure 4.11 Fundamental and second harmonic frequency as functions of time detected with the wedge method. 42

Figure 4.12 Specimens (all measures in mm) 43

Figure 4.13 Typical time signal with overlapping Lamb modes. 45

Figure 4.14 Spectrogram and dispersion curves. 47

Figure 4.15 Fundamental and second harmonic frequency as functions of time. 48

Figure 5.1 Relative nonlinearity value A_2/A_1^2 over the propagation distance for the two different aluminum alloys. 50

Figure 5.2 Fundamental and second harmonic frequency as functions of time after wave propagationed a distance of 200 mm. 52

Figure 5.3 Fundamental and second harmonic frequency as functions of time after wave propagationed a distance of 400 mm. 52

Figure 5.4 Spectrogram from measurement on a specimen with no plastic deformation. 53

Figure 5.5 Spectrogram from measurement on a specimen with plastic deformation. 53

Figure 5.6 Fundamental and second harmonic frequency as functions of time evaluated with wide Fourier Transformation window. 55

Figure 5.7 Fundamental and second harmonic frequency as functions of time evaluated with narrow Fourier Transformation window. 55

Figure 5.8 Stress–strain curve with load–points for the different specimens. . 56

Figure 5.9 A_1 over the plastic strain detected with the laser interferometer and a wide short–time Fourier transformation window. 59

Figure 5.10 A_2 over the plastic strain detected with the laser interferometer and a wide short–time Fourier transformation window. 59

Figure 5.11 A_1 over the plastic strain detected with the wedge method and a wide short–time Fourier transformation window. 60

Figure 5.12 A_2 over the plastic strain detected with the wedge method and a wide short–time Fourier transformation window. 60

Figure 5.13 Normalized relative value A_2/A_1^2 over the plastic strain detected with the laser interferometer and a wide short–time Fourier transformation window. 61

Figure 5.14 Normalized relative value A_2/A_1^2 over the plastic strain detected with the wedge method and a wide short–time Fourier transformation window. 62

Figure 5.15 A_1 over the plastic strain detected with the laser interferometer and a narrow short–time Fourier transformation window. 64

Figure 5.16 A_2 over the plastic strain detected with the laser interferometer and a narrow short–time Fourier transformation window. 64

Figure 5.17 A_1 over the plastic strain detected with the wedge method and a narrow short–time Fourier transformation window. 65

Figure 5.18 A_2 over the plastic strain detected with the wedge method and a narrow short–time Fourier transformation window. 65

Figure 5.19 Normalized relative value A_2/A_1^2 over the plastic strain detected with the laser interferometer and a narrow short–time Fourier transformation window. 67

Figure 5.20 Normalized relative value A_2/A_1^2 over the plastic strain detected with the wedge method and a narrow short–time Fourier transformation window. 68

Figure A.1 Time and Fourier domain signal representations 75

Figure A.2 STFT signal representations 75

Figure A.3 STFT with Hanning window 76

SUMMARY

In this thesis ultrasonic Lamb wave measurements are performed to detect material nonlinearity in aluminum sheets. When a Lamb wave propagates, higher harmonic wave fields are generated and under certain conditions the second harmonic is cumulative. When these conditions hold the Lamb waves are serviceable for material nonlinearity measurements. For generation, a wedge–transducer combination is used. The detection of the Lamb wave are performed with either a laser interferometer or a second wedge–transducer combination and the results are benchmarked. A short–time Fourier transformation (STFT) is applied to the detected signal to extract the amplitudes of the first and second harmonics. A relative ratio of the first and second harmonics is deduced from nonlinear wave theory to assign the nonlinearity of the material. To verify the capability of the measurement setup and to show that cumulative second harmonics are generated, measurements for different propagation distances are performed. Further measurements on plasticly deformed specimens are carried out to examine the change of the material nonlinearity as a function of plasticity.

CHAPTER I

INTRODUCTION

Ultrasonic wave measurements are a common way to monitor damage in materials. Classical nondestructive evaluation (NDE) techniques quantify microcracks in a material by measuring the scattered wave field. A new trend in nondestructive evaluation seeks to characterize the fatigue state of a component before the first microcracks are formed. Specifically the aerospace industry has the concern to continuously assess the fatigue state of a component. A promising technique is to measure the higher harmonics of a propagating ultrasonic wave generated from a wave guide material. The higher harmonics are excited by the material nonlinearity, which can be described with the nonlinear stress–strain relationship. Material nonlinearity is inherent in most solid materials. In addition, material nonlinearity can be induced by plastic deformation. Recent research has shown a significant increase in the measured material nonlinearity parameter with the accumulation of damage (plastic deformation) [7, 16, 21, 26]. This points out a potential for the development of a quantitative NDE measurement technique for fatigue state assessment with ultrasonic waves.

Compared to linear ultrasonic measurements, nonlinear measurements are more sensitive to detect changes in the material structure. The group velocity, phase velocity or attenuation do not change in a significant fashion with damage, since the induced changes in the material microstructure are much smaller than the typical wavelength of ultrasonic waves. The linear properties change less than 1 %, however the nonlinear acoustical properties change by more than 50 % [9]. Different ultrasonic wave types have been applied to measure nonlinearity in a material. Most often used are longitudinal, bulk waves [5, 32], but also Rayleigh [2, 5, 21] and Lamb waves [4, 16]

have been applied. Rayleigh and Lamb waves have the advantage that they propagate far distances. They are useful for long range inspection. However, Rayleigh waves propagate only on the surface and so are very sensitive to changes in surface condition. Lamb waves differ from the other wave types. They propagate in multiple modes. Because Lamb waves are dispersive, the modes additionally travel with different phase and group velocities. Therefore special conditions have to be meet so that a cumulative higher harmonic Lamb wave is generated [10, 12, 13, 14].

First in this work the performance of the experimental setup to measure the material nonlinearity in a material is verified. The Lamb waves are generated by a wedge–transducer combination. For the detection of the propagating Lamb waves, a non-contact laser interferometer and a second wedge–transducer combination have been applied. To verify the measurement setup, measurements are performed on two aluminum plates with different alloys. The cumulative effect of the second harmonic can be clearly observed. Additionally, the ratio of the measured nonlinearity is compared to the results of former measurement with longitudinal waves [32]. To show that a material nonlinearity increase can be detected with Lamb waves, measurements on plastically deformed specimens are performed. Finally, the signal processing is adapted to illustrate its influence on the measurements results.

This thesis first provides in Chapter 2 a review of the linear wave propagation theory in elastic solids. Further, important nonlinear wave propagation theory for this work is described. The absolute nonlinearity parameter β for the longitudinal wave propagation is derived. Because there exists no expression for a absolute nonlinearity parameter for Lamb waves, a relative nonlinearity value A_2/A_1^2 is deduced from β. In Chapter 3 the conditions for the excitation of cumulative second harmonics for Lamb waves are derived. Chapter 2 and Chapter 3 are the fundamentals for the experimental work. The experimental setup for the Lamb wave measurements is described in Chapter 4. The generation of the Lamb wave is explained. Further, the detection

of the propagating wave with a laser interferometer and with a wedge–transducer combination is illustrated. In the end of this chapter, an explanation of the short–time Fourier transformation and its application to the detected Lamb wave signal is given. With the transformed time signal, the separation of the modes amplitudes is possible. The limitation of the resolution of the short–time Fourier transformation is explained in detail in the appendix A. In Chapter 5, the results of the Lamb wave measurements are presented. A linear increase of the relative nonlinear value A_2/A_1^2 with growing propagation distance is verified and also a comparison of the ratio of two alloys with the results from longitudinal wave measurements is made. For the damage identification in material with Lamb waves, different specimens are loaded over yield so that plastic deformation occurred. With the Lamb wave measurements, a change of relative nonlinear value A_2/A_1^2 is observed. Furthermore, it can be shown the significant influence of the short–time Fourier transformation window adjustment on the measurements results. In the last chapter(Chapter 6) interpretation of the results and a summery is given. Moreover a outlook of further improvements and challenges of Lamb wave measurements is provided.

CHAPTER II

FUNDAMENTAL THEORY

This chapter gives an introduction in the fundamental theory of linear and nonlinear wave propagation. It is the necessary background for this research.

2.1 Linear wave propagation

The theory of linear wave propagation is well–known and –documented. Good sources are for instance Achenbach [1] and Graff [18]. The following sections will briefly describe the fundamental aspects of linear wave propagation. Additionally, wave phenomena like reflections are discussed. Finally, the key wave type for this research, the Lamb waves, will be explained.

2.1.1 Equations of motion

The equations of motion will be derived on a volume V at time t bounded by the surface S (see Figure 2.1). For this volume the force balance is set up. The time rate

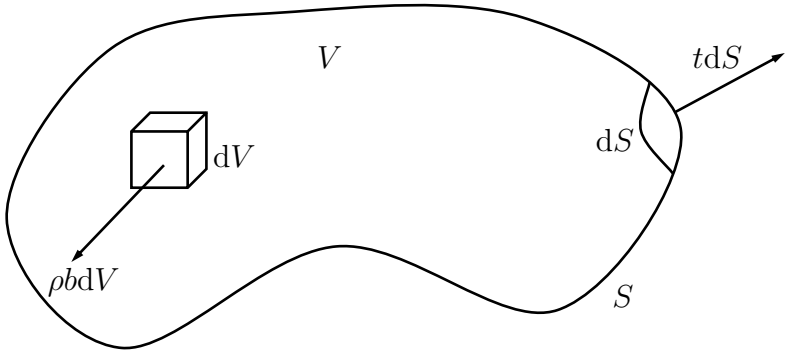

Figure 2.1: Momentum balance.

of the total momentum change for the collection of particles equals the vector sum of the external forces.

The total momentum change for the mass of the volume can be described as $\frac{\mathrm{d}}{\mathrm{d}t}\int \rho v_i \mathrm{d}V$. $\frac{\mathrm{d}}{\mathrm{d}t}$ is the material derivative of the integral. The momentum balance is given by the equation

$$\int_S t_i \mathrm{d}S + \int_V \rho b_i \mathrm{d}V = \frac{d}{dt}\int_V \rho v_i \mathrm{d}V, \tag{2.1}$$

where t_i are the surface tractions, b_i are the body forces and v_i are the velocity. With the substitution of surface traction by the Cauchy formula

$$t_i = \sigma_{ij} n_j \tag{2.2}$$

in equation (2.1) and transformation of the surface integral using the Gauss' theorem gives

$$\int_V [\sigma_{ij,j} + \rho b_i - \rho \dot{v}_i] \mathrm{d}V = 0. \tag{2.3}$$

The material derivative inside the integral is converted by the Reynolds formula. Since equation (2.3) valid for any arbitrary volume the integral can be left, which leads to the Cauchy's equations of motion.

$$\sigma_{ij,j} + \rho b_i = \rho \dot{v}_i \ . \tag{2.4}$$

The stress tensor σ_{ij} in this equation is symmetric.

Representing the equations of motion only in terms of the displacements u_i and with the Hooke's law for a homogeneous, isotropic and linear elastic medium leads to

$$\sigma_{ij} = \lambda \epsilon_{kk} \delta_{ij} + 2\mu \epsilon_{ij}, \tag{2.5}$$

where ϵ_{ij} is expressed by the strain tensor displacements u_i relation

$$\epsilon_{ij} = \frac{1}{2}(u_{i,j} + u_{j,i}) \ . \tag{2.6}$$

From equation (2.5) we can derive the Navier's equation of motion. The equation is represented in the indical notation and in a form with vector operators.

$$\mu u_{i,jj} + (\lambda + \mu) u_{j,ji} = \rho \ddot{u}_i \tag{2.7}$$

$$\mu \nabla^2 \mathbf{u} + (\lambda + \mu) \nabla \nabla \cdot \mathbf{u} = \rho \ddot{\mathbf{u}}, \tag{2.8}$$

where λ and μ are the Lamé constants. In this expressions the body forces are neglected.

The Helmholtz decomposition (2.9) is applied to uncouple the coupled partial differential equation (2.8)

$$\mathbf{u} = \nabla\varphi + \nabla \times \boldsymbol{\psi}. \tag{2.9}$$

where the components of the displacement u are described in four potential functions φ, ψ_1, ψ_2 and ψ_3. Another constraint is necessary to guarantee the uniqueness of the solution:

$$\nabla \cdot \boldsymbol{\psi} = 0. \tag{2.10}$$

Applying the Helmholtz decomposition (2.9) on the displacement equations of motion (2.8) gives two uncoupled wave equations expressed in terms of the displacement potentials φ and $\boldsymbol{\psi}$:

$$\nabla^2\varphi = \frac{1}{c_{\mathrm{L}}^2}\ddot{\varphi}, \tag{2.11}$$

$$\nabla^2\boldsymbol{\psi} = \frac{1}{c_{\mathrm{T}}^2}\ddot{\boldsymbol{\psi}}. \tag{2.12}$$

c_{L} defined the wave speed of the longitudinal wave (also called dilatational, irrotational, pressure or P–wave), where c_{T} is the wave speed of the vertically and horizontally polarized shear waves (also called transverse, rotational, distortional or S–waves). Expressed with the material properties, the wave speeds are given by

$$c_{\mathrm{L}}^2 = \frac{\lambda + 2\mu}{\rho} \tag{2.13}$$

and

$$c_{\mathrm{T}}^2 = \frac{\mu}{\rho}\ . \tag{2.14}$$

Substitute the potentials in the wave equations (2.11)–(2.12) by the displacements or the strains, the equations will still be valid.

Note, that always $c_{\mathrm{L}} > c_{\mathrm{T}}$. Further the Lamé constants λ and μ can be expressed with Young's modulus E and Poisson's ratio ν by the relation

$$\lambda = \frac{E\nu}{(1+\nu)(1-2\nu)} , \tag{2.15}$$

$$\mu = \frac{E}{2(1+\nu)} . \tag{2.16}$$

2.1.2 Wave phenomena

All in this section discussed wave phenomena are based on the plane wave assumption, i.e., that we assume the wave has constant properties (ϵ, σ, u) on a plane perpendicular to its direction of propagation $\mathbf{p}$ (propagating vector). The mathematical expression of a plane wave is

$$\mathbf{u} = \mathbf{d} f(\mathbf{x} \cdot \mathbf{p} - ct) , \tag{2.17}$$

In this equation $\mathbf{d}$ and $\mathbf{u}$ are unit vectors. They defining the direction of particle motion and propagation. c being either the longitudinal wave speed c_{L} or the transverse wave speed c_{T}. Insert of (2.17) into equation of motion (2.8) follows

$$(\mu - \rho c^2)\mathbf{d} + (\lambda + \mu)(\mathbf{p} \cdot \mathbf{d})\mathbf{p} = 0 . \tag{2.18}$$

$\mathbf{p}$ and $\mathbf{d}$ are two different unit vectors, so we can get two different solutions from the equation (2.18). The first solution is $\mathbf{d} = \pm\mathbf{p}$, the second is $\mathbf{p} \cdot \mathbf{d} = 0$. The solutions forming the basis of wave propagation. Next we discuss this two cases:

(1) If $\mathbf{d} = \pm\mathbf{p}$ we obtain $\mathbf{p} \cdot \mathbf{d} = \pm 1$. With (2.13) and (2.18) gives $c = c_{\mathrm{L}}$. Since $\mathbf{d}$ and $\mathbf{p}$ are linearly dependent. This describes the particle movement parallel to the direction of the wave propagation and is denoted as a longitudinal or P–wave.

(2) If $\mathbf{p} \cdot \mathbf{d} = 0$ we obtain with (2.14) and (2.18) that $c = c_{\mathrm{T}}$. The direction of motion is normal to the direction of the wave propagation. This wave is denoted as

transverse or S–wave. If a two–dimensional plane of propagation is considered (for example, the (x_1, x_2)-plane), a wave with an in–plane displacement (in the (x_1, x_2)-plane) is called SV–wave (vertically polarized), while a wave with out–of–plane displacement (in the x_3–direction) is called SH–wave (horizontally polarized).

In a homogeneous, isotropic material, transverse and longitudinal wave speeds are independent of frequency, therefore they are nondispersive.

2.1.3 Wave reflection on a plane interface

As derived so far, the different wave types propagating independently from each other. But, if the medium is finite in the direction of propagation, reflections and coupling will appear on the boundary. To meet the boundary condition, an incident P–wave is mostly reflected as both P–and SV–wave at a stress free boundary ($\sigma_{22} = 0$ and $\sigma_{21} = 0$). Likewise, on a stress free boundary an incident SV–wave is normally reflected as both SV–and P–waves. This effect is known as mode conversion. A reflection of P–wave on a free surface is displayed in Figure 2.2a, a reflection of a SV–wave is displayed in Figure 2.2b.

A common way to define a displacement field of a harmonic wave in the (x_1, x_2)–plane (propagating in infinite media, plane–strain case) is

$$\mathbf{u}^{(n)} = A_n \mathbf{d}^{(n)} \exp\left[\imath k_n (x_1 p_1^{(n)} + x_2 p_2^{(n)} - c_n t)\right] , \tag{2.19}$$

where n denotes the wave characteristics (longitudinal or transverse) and $k_n = \frac{\omega}{c_n}$ is called the wavenumber of the nth wave with the respective wave speeds c_n. With this representation of a wave field, the constraint of equal angular frequency ω for the incident and the reflected waves and the boundary conditions it is possible to obtain the relationship between the angle of the incident and the angles of the reflected waves (Table 2.1). To get a non–trivial solution for the amplitudes A_n, the angles of

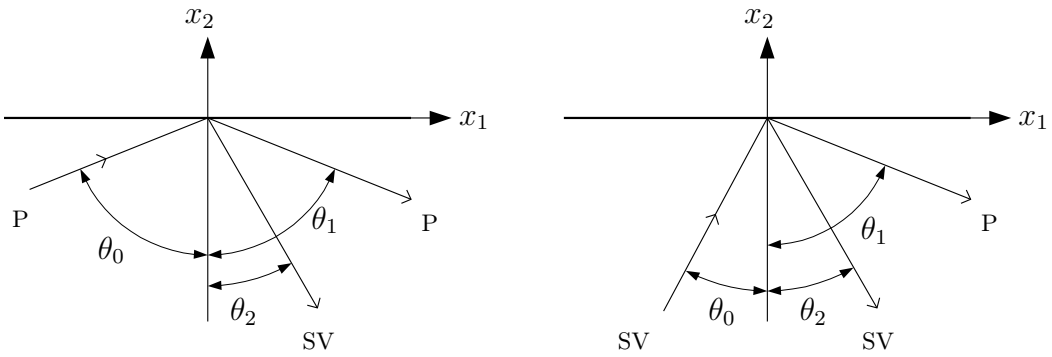

Figure 2.2: Wave reflections. (a) Reflection of a P–wave. (b) Reflection of a SV–wave.

Table 2.1: Angle relations for reflection on a stress–free surface.

incident θ_0	reflected P θ_1	reflected SV θ_2
P	$\theta_1 = \theta_0$	$\sin\theta_2 = (c_\mathrm{T}/c_\mathrm{L})\sin\theta_0$
SV	$\sin\theta_1 = (c_\mathrm{L}/c_\mathrm{T})\sin\theta_0$	$\theta_2 = \theta_0$

incident and reflected waves θ_0, θ_1 and θ_2 in Figure 2.2 have to satisfy Snell's law:

$$k_0 \sin\theta_0 = k_1 \sin\theta_1 = k_2 \sin\theta_2 \ . \tag{2.20}$$

There exist two exceptions for mode conversion: First case, the incidence wave is normal to the reflection surface. So $\theta_0 = 0$ and the waves are reflected as themselves. The second case occurs if the angle θ_0 is greater than a critical angle

$$\theta_\mathrm{critical} = \arcsin\frac{c_\mathrm{T}}{c_\mathrm{L}} \ , \tag{2.21}$$

only an SV–wave is reflected. The P–wave portion of the reflected signal degenerates into a Rayleigh surface wave, which is a specific type of two–dimensional harmonic wave.

2.1.4 Lamb waves

Lamb waves are a typical representative of a guided wave. A wave guide is a body with at least one, but normally two boundaries. Figure 2.3 shows the reflection of

the waves at the interfaces. This leads to a multiple reflection on the surfaces in propagation direction. With every reflection mode conversion occurs and more waves propagate in the waveguide, which ends in an interference pattern of a standing wave in x_2-direction and a traveling wave in x_1-direction.

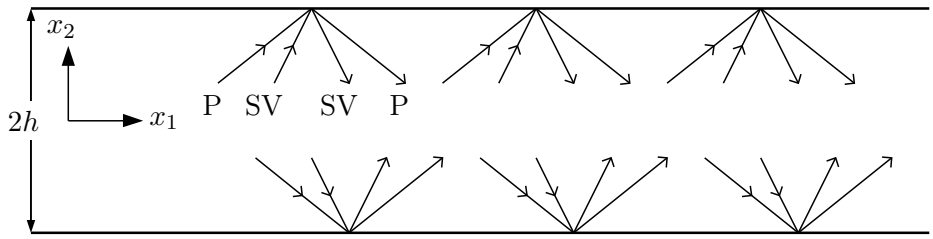

Figure 2.3: Multiple reflections in a waveguide.

The wave equation in potential from is used in order to model the phenomenon of guided waves:

$$\frac{\partial^2\varphi}{\partial x_1^2}+\frac{\partial^2\varphi}{\partial x_2^2} = \frac{1}{c_L^2}\frac{\partial^2\varphi}{\partial t^2} \tag{2.22}$$

$$\frac{\partial^2\phi}{\partial x_1^2}+\frac{\partial^2\phi}{\partial x_2^2} = \frac{1}{c_T^2}\frac{\partial^2\phi}{\partial t^2} \tag{2.23}$$

We consider the complex potentials solution as[30]

$$\varphi = \Phi(x_2)e^{\imath(kx_1-\omega t)} \tag{2.24}$$

$$\psi = \Psi(x_2)e^{\imath(kx_1-\omega t)}. \tag{2.25}$$

Insert (2.24) and (2.25) in (2.22) and (2.23) we obtain

$$\varphi(x_2) = A_1 sin(px_2) + A_2 cos(px_2) \tag{2.26}$$

$$\psi(x_2) = B_1 sin(qx_2) + B_2 cos(qx_2) \tag{2.27}$$

with

$$p^2 = \frac{\omega^2}{c_{\mathrm{L}}^2} - k^2, \qquad q^2 = \frac{\omega^2}{c_{\mathrm{T}}^2} - k^2. \tag{2.28}$$

The additionally assumption for x_1–direction as propagation direction and plane strain stress free boundaries at $x_2 = \pm h$ gives the Rayleigh–Lamb frequency equations as shown Achenbach [1]:

$$\frac{\tan(qh)}{\tan(ph)} = -\frac{4k^2pq}{(q^2-k^2)^2} \tag{2.29}$$

and

$$\frac{\tan(qh)}{\tan(ph)} = -\frac{(q^2-k^2)^2}{4k^2pq}\,. \tag{2.30}$$

Equation (2.29) declares the symmetric Lamb modes and equation (2.30) declares the antisymmetric Lamb modes. Symmetric and antisymmetric stays for the displacement distribution over the plate thickness with respect to the propagation direction $\mathbf{p}$, here the x_1–direction. In Figure 2.4 the in–plane and out–of–plane displacement distribution for the first three symmetric and antisymmetric modes are sketched. The tickness of the waveguide is defined as $2h$. Every Lamb mode has a frequency ω and a specific phase velocity $c_{\mathrm{ph}} = \frac{\omega}{k}$. Lamb waves are dispersive and the mode velocities are dependent on the frequency. Today there exist only numerical solution for the Rayleigh-Lamb equation. Figure 2.5 shows the calculated mode curves illustrated in the normalized frequency over the phase velocity. The symmetric modes obtained from equation (2.29) are labeled $s_i, i = 0...4$, the antisymmetric modes obtained from equation (2.30) are labeled $a_i, i = 0...4$. First, the numerical solution for all modes in the (ω, k)–domain (and with $f = \frac{\omega}{2\pi}$ in the (f, k)–domain, respectively) is computed, and afterward f is differentiated partially with respect to the wave number k for all modes. The derivative, representing the group velocity $c_{\mathrm{g}}(f)$, is

$$c_{\mathrm{g}}(f) = 2\pi\frac{\partial f}{\partial k}. \tag{2.31}$$

The group velocity accounts for the velocity of the energy propagating with the wave and comes from the superposition of waves. In general the group velocity c_{g} is smaller than the phase velocity c_{ph}. The phase velocity c_{ph} is defined as $c_{\mathrm{ph}} = \frac{\omega}{k}$ and describes

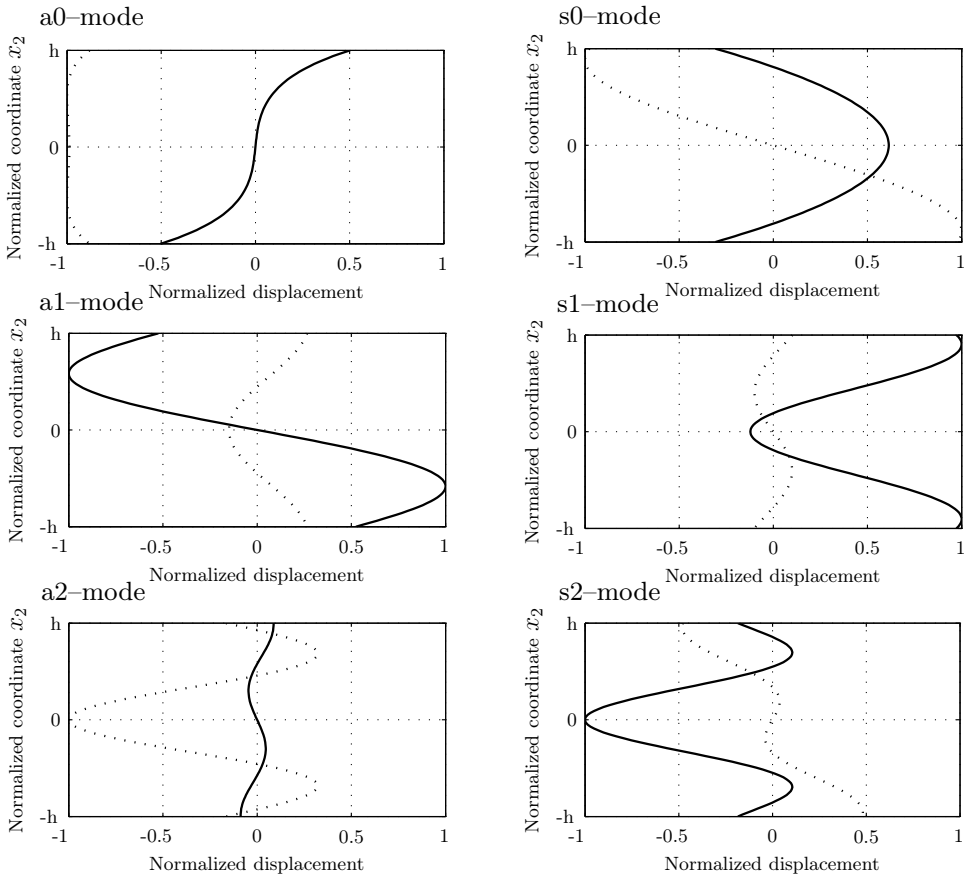

Figure 2.4: In–plane (solid line) and out–of–plane (dotted line) displacement distribution for a aluminum plate normalized with wave number k=5.

the velocity of points with constant phase. Note, that for nondispersive , i.e. infinitely linearly elastic media, group and phase velocity are equal.

The energy slowness $sl_e(f)$ can be derived form the equation (2.31) by

$$sl_e(f) = \frac{1}{c_g(f)}. \tag{2.32}$$

For the theoretical solution in the time–frequency domain, the relationship

$$t(f) = \frac{sl_e(f)}{d} \tag{2.33}$$

is used. Time t represents the expected arrival time for a specific mode at frequency f with a propagation distance of d between sender and receiver.

Figure 2.6 present a theoretical Lamb wave for a plate with 1mm thickness, calculated with a existing and modified MATLAB code. The waveform results from the

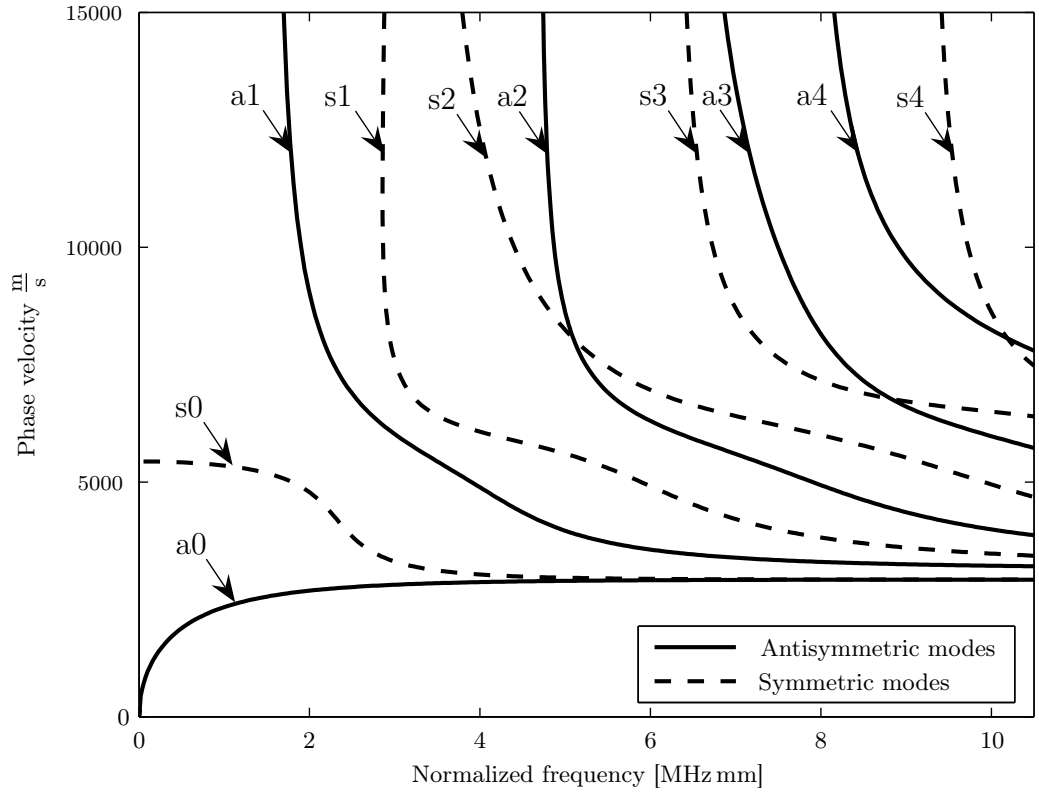

Figure 2.5: Theoretical solution in the phase velocity – frequency domain (dispersion curves).

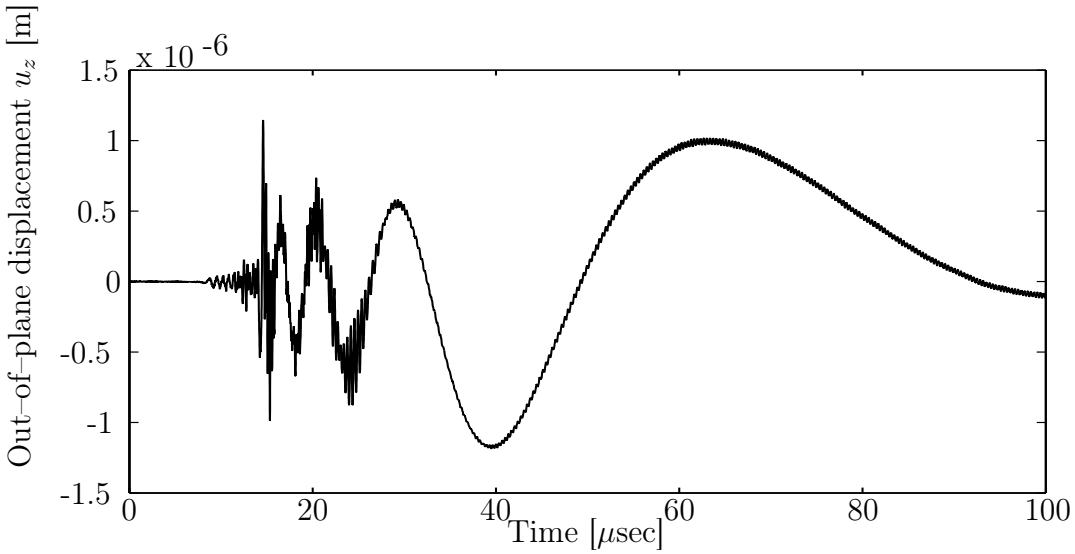

Figure 2.6: Theoretical solution for the Lamb wave.

superposition of the first six symmetric and anti–symmetric modes with a modeled sampling frequency of 100 MHz. More details about the implementation of dispersion curves and normal mode expansion can be found in Pao [31].

2.2 Nonlinear wave propagation

In this sub chapter the one–dimensional nonlinear wave propagation will be described. Figure 2.7 illustrate the effect of the nonlinearity of a solid on a propagating wave. While in a linear medium only the exited frequency of the wave will be detected after transverse through the material, higher harmonic frequencies will occur in a nonlinear medium. These higher harmonic frequencies are integer multiples of the exited fundamental frequency. The wave will be distorted by the material nonlinearity as

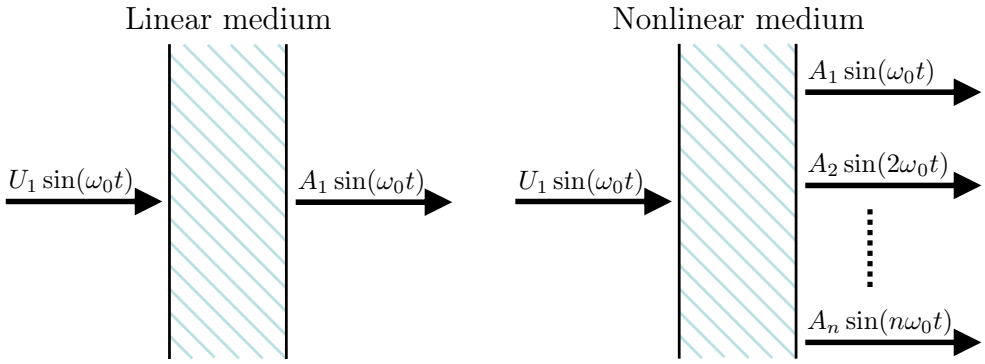

Figure 2.7: Linear and nonlinear wave propagation in a solid.

it propagates [22, 6]. The material nonlinearity is generated by either material inherent or damages due to plastic deformation. The inherent nonlinearity are caused for example by lattice anharmonicities, precipitates or vacancies. The damage caused nonlinearity is generated from dislocations or microcracks.

2.3 Nonlinearity parameter β

A nonlinearity parameter β will be induced, a quantitative parameter for the degree of nonlinearity of the medium. It is experimentally proved, that β depends on the material properties [3]. Additionally, the value of β changes, if plastic deformation damaged the material [20]. A relationship between the parameter β and of the amplitudes of the fundamental and second harmonic frequency is derived. The detailed derivation of β can be found in [7]. This expression is only valid for longitudinal waves measurements and is used for the definition of the relative nonlinearity ratio A_2/A_1^2 for the Lamb waves. The introduction of the nonlinearity ratio A_2/A_1^2 and the derived conditions for the cumulative second harmonic wave field are the theoretical background for experiments in this thesis.

Longitudinal stress perturbation $\bar{\sigma}$ due to a propagating ultrasonic wave creates a longitudinal strain

$$\epsilon = \epsilon_{\mathrm{e}} + \epsilon_{\mathrm{pl}}\,, \tag{2.34}$$

where ϵ_{e} stays for the elastic strain component and ϵ_{pl} stays for the plastic strain component associated with the motion of dislocations in the dipole configuration. The nonlinear Hooke's law (quadratic nonlinear approach) gives the relation between stress perturbation $\bar{\sigma}$ and elastic strain component ϵ_{e} by

$$\bar{\sigma} = A_2^{\mathrm{e}}\epsilon_{\mathrm{e}} + \frac{1}{2}A_3^{\mathrm{e}}\epsilon_{\mathrm{e}}^2 + \text{higher order terms (h.o.t.)} \tag{2.35}$$

or

$$\epsilon_{\mathrm{e}} = \frac{1}{A_2^{\mathrm{e}}}\bar{\sigma} - \frac{1}{2}\frac{A_3^{\mathrm{e}}}{(A_2^{\mathrm{e}})^3}\bar{\sigma}^2 + \text{h.o.t.}\quad . \tag{2.36}$$

A_2^{e} and A_3^{e} account for the Huang coefficients [24] and denote also the initial stress configuration.

As described in [7], the correlation between the stress perturbation $\bar{\sigma}$ and the plastic

strain component ϵ_{pl} can be achieved by account the dipolar forces. For edge dislocation pairs with opposite polarity, the force per unit length along the glide plane is defined as

$$\bar{F}_{x_1} = -\frac{Gb^2}{2\pi(1-\nu)} \frac{x_1(x_1^2 - x_2^2)}{(x_1^2 + x_2^2)^2}\,, \tag{2.37}$$

where G is the shear modulus, b is the Burgers vector, ν is Poisson's ratio and x_1 and x_2 are the Cartesian coordinates of one dislocation pair relative to the other. It is supposed, the motion in dipole pairs taking place just along parallel slip planes separated by the so–called equilibrium dipole height $x_2 = h$, where h is the dipole height. The equilibrium at this height can be expressed by

$$\bar{F}_{x_1} + bR\bar{\sigma} = 0. \tag{2.38}$$

where R is the longitudinal–to–shear conversion factor or also denoted as Schmid factor along the slip planes.

In addition the correlation between the plastic strain component ϵ_{pl} and the relative dislocation displacement $\xi = x - h$ can be write

$$\epsilon_{\mathrm{pl}} = \Omega \Lambda^{\mathrm{dp}} b \xi. \tag{2.39}$$

with Ω is refered to the conversion factor from the dislocation displacement in the slip plane to a longitudinal displacement along an arbitrary direction and Λ^{dp} is the dipole density.

It follows from the equations (2.38)–(2.39) and a power series expansion from (2.37) that

$$\bar{\sigma} = A_2^{\mathrm{dp}} \epsilon_{\mathrm{pl}} + \frac{1}{2} A_3^{\mathrm{dp}} \epsilon_{\mathrm{pl}}^2 + \text{h.o.t.} \quad , \tag{2.40}$$

where

$$\begin{aligned} A_2^{\mathrm{dp}} &= -\left(\frac{G}{4\pi\Omega R \Lambda^{\mathrm{dp}} h^2 (1-\nu)} \right), \\ A_3^{\mathrm{dp}} &= \left(\frac{G}{4\pi\Omega^2 R (\Lambda^{\mathrm{dp}})^2 h^3 (1-\nu) b} \right). \end{aligned} \tag{2.41}$$

And the inverse relation for $\epsilon_{\rm pl}$ is

$$\epsilon_{\rm pl} = \frac{1}{A_2^{\rm dp}}\bar{\sigma} - \frac{1}{2}\frac{A_3^{\rm dp}}{(A_2^{\rm dp})^3}\bar{\sigma}^2 + \text{h.o.t.} \quad . \tag{2.42}$$

Further, replace $\epsilon_{\rm e}$ and $\epsilon_{\rm pl}$ in equation (2.34) by (2.36) and (2.42) gives the longitudinal strain as

$$\epsilon = \left(\frac{1}{A_2^{\rm e}} + \frac{1}{A_2^{\rm dp}}\right)\bar{\sigma} - \frac{1}{2}\left(\frac{A_3^{\rm e}}{(A_2^{\rm e})^3} + \frac{A_3^{\rm dp}}{(A_2^{\rm dp})^3}\right)\bar{\sigma}^2 + \text{h.o.t.} \quad , \tag{2.43}$$

with the inverse relation

$$\bar{\sigma} = A_2^{\rm e}\left[\epsilon - \frac{1}{2}\left(\frac{A_3^{\rm e}}{A_2^{\rm e}} + \frac{A_3^{\rm dp}(A_2^{\rm e})^2}{(A_2^{\rm dp})^3}\right)\epsilon^2 + \text{h.o.t.}\right] . \tag{2.44}$$

The one–dimensional wave equation with respect to the Lagrangian coordinate X can be written with the result before as

$$\rho\frac{\partial^2\epsilon}{\partial t^2} = \frac{\partial^2\bar{\sigma}}{\partial X^2} \ . \tag{2.45}$$

(2.44) in (2.45) leads in the strain–based nonlinear wave equation

$$\frac{\partial^2\epsilon}{\partial t^2} - c^2\frac{\partial^2\epsilon}{\partial X^2} = \frac{c^2\beta}{A_2^{\rm e}}\left[\epsilon\frac{\partial^2\epsilon}{\partial X^2} + \left(\frac{\partial\epsilon}{\partial X}\right)^2\right], \tag{2.46}$$

where

$$\begin{aligned} c &= \sqrt{\frac{A_2^{\rm e}}{\rho}}, \\ \beta &= \beta_{\rm e} + \beta_{\rm dp}, \\ \beta_{\rm e} &= -\frac{A_3^{\rm e}}{A_2^{\rm e}}, \\ \beta_{\rm dp} &= \frac{16\pi\Omega R^2\Lambda_{\rm dp}h^3(1-\nu)^2(A_2^{\rm e})^2}{G^2 b} \, . \end{aligned} \tag{2.47}$$

The Huang coefficients are often given in terms of the higher elastic constants, so that $A_1^{\rm e} = C_1$ with C_1 equal to the initial stress, $A_2^{\rm e} = C_1 + C_{11}$ and $A_3^{\rm e} = 3C_{11} + C_{111}$. Assuming that the initial stress is zero, means $C_1 = 0$, the portion of β describing

the nonlinearity contribution from lattice elasticity can be expressed in terms of the higher order elastic constants as

$$\beta_e = -\left(3 + \frac{C_{111}}{C_{11}}\right) \ . \tag{2.48}$$

Only the displacement can be measured experimentally. The nonlinearity parameter β in terms of displacement u is

$$\rho \frac{\partial^2 u}{\partial t^2} = \frac{\partial^2 \bar{\sigma}}{\partial X^2}. \tag{2.49}$$

Insert (2.44) in (2.49) leads in a nonlinear wave equation expressed in displacement representation

$$\frac{\partial^2 u}{\partial t^2} = c^2 \left[1 - \beta \frac{\partial u}{\partial X}\right] \frac{\partial^2 u}{\partial X^2} \, . \tag{2.50}$$

Suppose an sinusoidal input wave in a form $u_0 \cos(kX - \omega t)$ the solution of (2.50) is derived by

$$u = \frac{1}{8}\beta k^2 u_0^2 X + u_0 \cos(kX - \omega t) - \frac{1}{8}\beta k^2 u_0^2 X \cos[2(kX - \omega t] + \text{ h.o.t. } . \tag{2.51}$$

Define $A_1 = u_0$ and $A_2 = \frac{1}{8}\beta k^2 u_0^2 X$ as amplitudes for fundamental and second harmonic wave and neglect the higher order terms of (2.51), the nonlinear parameter β can be expressed by

$$\beta = \frac{8}{k^2 X}\left(\frac{A_2}{A_1^2}\right). \tag{2.52}$$

With substitute the wavenumber with the expression $k = \frac{\omega}{c}$ defines an alternative form of (2.52)

$$\beta \ = \ 8\frac{c^2}{\omega^2 X}\left(\frac{A_2}{A_1^2}\right). \tag{2.53}$$

Because there exist at the moment no expression for absolute nonlinearity parameter β for Lamb waves, the relative nonlinear value A_2/A_1^2 is used in the experiments to determine the material nonlinearity. This value is proportional to the absolute

nonlinearity parameter β. Hence the ratio A_2/A_1^2 is a relative value it can only be applied to determine the difference of nonlinearity of various materials or the changes of the nonlinearity due to plastic deformation. In the experiments of this thesis the amplitudes A_1 and A_2 are the from the measurement system detected normal surface velocities of the waveguide.

CHAPTER III

EXCITATION OF CUMULATIVE SECOND HARMONICS IN LAMB WAVES

The objective of this work is to generate and detect second harmonics of propagating Lamb waves for nondestructive evaluation. To be possible to reliably measure the second harmonic, the generation must be cumulative over the propagation distance. But certain conditions must be satisfied that cumulative second harmonic Lamb waves are exited. Deng, Hamilton and further assigned these conditions [12, 13, 14] and proofed this experimentally [3, 15, 16]. The conditions has to be satisfied in the experimental work.

3.1 Theoretical fundamentals for cumulative second harmonic

In general, second harmonics of a propagating Lamb wave are not cumulative. However, under certain conditions cumulative second harmonics are generated. The conditions will be derived in this section.

The Lamb wave propagates with four partial waves: two longitudinal waves and two transverse waves. The generation of the second harmonic is due to the nonlinearity of the waveguide material and the following nonlinear interaction of the four partial bulk waves. The nonlinear wave equation for homogeneous solid with no attenuation and no dispersion expressed in terms of displacement vector $\mathbf{u}$ is

$$\rho\frac{\partial^2\mathbf{u}}{\partial t^2} - \left(\lambda + \frac{4\mu}{3}\right)\nabla(\nabla\cdot\mathbf{u}) + \mu\nabla\times(\nabla\times\mathbf{u}) = \mathbf{F}(\mathbf{u})\,, \tag{3.1}$$

where ρ is the solid's density, λ and μ are the Lamé constants. The right hand side of the wave equation is quadric and the displacement vector $\mathbf{u}$ has normally a finite amplitude, so the right side will be smaller than the linear left hand side. To get the solution for (3.1), $\mathbf{u}$ will be expanded in the fundamental and second harmonic frequency component

$$\mathbf{u} = \mathbf{u}^{(1)} + \mathbf{u}^{(2)}. \tag{3.2}$$

Replace $\mathbf{u}$ in equation (3.1) we obtain to two linear equations:

$$\rho\frac{\partial^2\mathbf{u}^{(1)}}{\partial t^2} - \left(\lambda + \frac{4\mu}{3}\right)\nabla(\nabla\cdot\mathbf{u}^{(1)}) + \mu\nabla\times(\nabla\times\mathbf{u}^{(1)}) = 0, \tag{3.3}$$

$$\rho\frac{\partial^2\mathbf{u}^{(2)}}{\partial t^2} - \left(\lambda + \frac{4\mu}{3}\right)\nabla(\nabla\cdot\mathbf{u}^{(2)}) + \mu\nabla\times(\nabla\times\mathbf{u}^{(2)}) = \mathbf{F}(\mathbf{u}^{(1)}). \tag{3.4}$$

$\mathbf{F}(\mathbf{u}^{(1)})$ comes from $\mathbf{F}(\mathbf{u})$, where $\mathbf{u}$ is replaced by $\mathbf{u}^{(1)}$. A Cartesian coordinate system is selected. The origin is placed in the center of the plate. The x_2–axis is perpendicular to the plate boundaries and the x_3–axis is parallel to the plate boundaries. The displacement vectors $\mathbf{u}$ of the four partial bulk waves lie in the (x_1, x_2)–plane. With regard of Snell's law for the four partial Lamb waves, propagating with frequency f and angular frequency ω, the solution can be derived from (3.3)

$$\begin{aligned}
\mathbf{u}_{\mathrm{T}1} &= u_{\mathrm{T}1}(\hat{x}_1\times\mathbf{K}^0_{\mathrm{T}1})\exp[\imath\mathbf{K}_{\mathrm{T}1}\cdot\mathbf{r}_1 - \imath\omega t],\\
\mathbf{u}_{\mathrm{L}1} &= u_{\mathrm{L}1}\mathbf{K}^0_{\mathrm{L}1}\exp[\imath\mathbf{K}_{\mathrm{L}1}\cdot\mathbf{r}_1 - \imath\omega t],\\
\mathbf{u}_{\mathrm{T}2} &= u_{\mathrm{T}2}(\mathbf{K}^0_{\mathrm{T}2}\times\hat{x}_1)\exp[\imath\mathbf{K}_{\mathrm{T}2}\cdot\mathbf{r}_2 - \imath\omega t],\\
\mathbf{u}_{\mathrm{L}2} &= u_{\mathrm{L}2}\mathbf{K}^0_{\mathrm{L}2}\exp[\imath\mathbf{K}_{\mathrm{L}2}\cdot\mathbf{r}_2 - \imath\omega t],
\end{aligned} \tag{3.5}$$

with

$$\begin{aligned}
\mathbf{K}_{Pm}\cdot\mathbf{r}_m &= kx_3 + (-1)^{m-1}\alpha_P k x_2, \quad m = 1, 2,\\
K_P &= \frac{\omega}{V_P} = |\mathbf{K}_{P1}| = |\mathbf{K}_{P2}|, \quad k = K_P\sin\theta_P,\\
\alpha_P k &= K_P\cos\theta_P,\\
\alpha_P &= \sqrt{\left(\frac{c^2_{\mathrm{ph}}}{c^2_P}\right) - 1}, \quad P = \mathrm{L}, \mathrm{T}.
\end{aligned} \tag{3.6}$$

The longitudinal and transverse wave vectors for the partial bulk waves are $\mathbf{K}_{\mathrm{L}m}$ and $\mathbf{K}_{\mathrm{T}m}$ $(m = 1, 2)$. θ_{T} and θ_{L} are the angle between the wave vectors and the x_2–axis, $\hat{x}_1$ stays for the unit vector in x_1–direction. k represents the components of $\mathbf{K}_{\mathrm{L}m}$ and $\mathbf{K}_{\mathrm{T}m}$ in x_3–direction, $u_{\mathrm{L}m}$ and $u_{\mathrm{T}m}$ $(m = 1, 2)$ accounts for the partial longitudinal and transverse waves amplitudes. Finally, K_P $(P = \mathrm{L}, \mathrm{T})$ denotes the magnitude of $\mathbf{K}_{Pm}$, c_P refers to the longitudinal or transverse velocity and c_{ph} to the phase velocity of the lamb wave.

The boundary conditions of the surfaces $x_2 = \pm h$ are, that the stress $T_{x_2x_2}(\pm h) = T_{x_2x_3}(\pm h) = 0$. So the four wave amplitudes $u_{\mathrm{L}m}$ and $u_{\mathrm{T}m}$ $(m = 1, 2)$ can be determined. One can write

$$\imath k[M(\omega, k)] \begin{bmatrix} \mathbf{u}_{\mathrm{L}1} \\ \mathbf{u}_{\mathrm{T}1} \\ \mathbf{u}_{\mathrm{L}2} \\ \mathbf{u}_{\mathrm{T}2} \end{bmatrix} = 0 \tag{3.7}$$

with the coefficient matrix

$$[M(\omega, k)] = \begin{bmatrix} 2\mu\cos\theta_{\mathrm{L}}R_{\mathrm{L}+} & (\alpha_{\mathrm{T}}^2 - 1)\mu\sin\theta_{\mathrm{T}}R_{\mathrm{T}+} & -2\mu\cos\theta_{\mathrm{L}}R_{\mathrm{L}-} & -(\alpha_{\mathrm{T}}^2 - 1)\mu\sin\theta_{\mathrm{T}}R_{\mathrm{T}-} \\ 2\mu\cos\theta_{\mathrm{L}}R_{\mathrm{L}-} & (\alpha_{\mathrm{T}}^2 - 1)\mu\sin\theta_{\mathrm{T}}R_{\mathrm{T}-} & -2\mu\cos\theta_{\mathrm{L}}R_{\mathrm{L}+} & -(\alpha_{\mathrm{T}}^2 - 1)\mu\sin\theta_{\mathrm{T}}R_{\mathrm{T}+} \\ M_{31}R_{\mathrm{L}+} & M_{32}R_{\mathrm{T}+} & M_{31}R_{\mathrm{L}-} & M_{32}R_{\mathrm{T}-} \\ M_{31}R_{\mathrm{L}-} & M_{32}R_{\mathrm{T}-} & M_{31}R_{\mathrm{L}+} & M_{32}R_{\mathrm{T}+} \end{bmatrix}.$$

with $R_{\mathrm{L}\pm} = \exp(\pm\imath\alpha_{\mathrm{L}}kh)$, $R_{\mathrm{T}\pm} = \exp(\pm\imath\alpha_{\mathrm{T}}kh)$, $M_{31} = (C_{11}\alpha_{\mathrm{L}}^2 + C_{12})\sin\theta_{\mathrm{L}}$ and $M_{32} = (C_{12} - C_{11})\cos\theta_{\mathrm{T}}$ with $C_{11} = \lambda + \frac{4\mu}{3}$ and $C_{12} = \lambda - \frac{2\mu}{3}$. To derive a nontrivial solution from equation (3.7), the determinant of $[M(\omega, k)]$ must be zero. From this condition the two dispersion equations of Lamb mode propagation arise

$$\frac{\tan(\alpha_{\mathrm{T}}kh)}{\tan(\alpha_{\mathrm{L}}kh)} = -\frac{4\alpha_{\mathrm{T}}\alpha_{\mathrm{L}}}{\left(2 - \frac{c_{\mathrm{ph}}^2}{c_{\mathrm{T}}^2}\right)^2}, \tag{3.8}$$

$$\frac{\tan(\alpha_{\mathrm{T}}kh)}{\tan(\alpha_{\mathrm{L}}kh)} = -\frac{\left(2 - \frac{c_{\mathrm{ph}}^2}{c_{\mathrm{T}}^2}\right)^2}{4\alpha_{\mathrm{T}}\alpha_{\mathrm{L}}}, \tag{3.9}$$

where kh represents the normalized thickness of the solid plate. Insert (3.8) in (3.7) leads to the symmetric Lamb mode propagation condition

$$u_{P1} = u_{P2}, \quad P = \mathrm{L}, \mathrm{T} \tag{3.10}$$

while insert (3.9) in (3.7) the antisymmetric equivalent

$$u_{P1} = -u_{P2}, \quad P = \mathrm{L}, \mathrm{T} \tag{3.11}$$

is obtained.

Since we examine the interaction of multiple waves, the fundamental displacement field $\mathbf{u}^{(1)}$ can be expressed as the superposition of the four partial bulk waves of Lamb propagation with

$$\mathbf{u}^{(1)} = \mathbf{u}_{\mathrm{T}1} + \mathbf{u}_{\mathrm{L}1} + \mathbf{u}_{\mathrm{T}2} + \mathbf{u}_{\mathrm{L}2}. \tag{3.12}$$

Set (3.12) in $\mathbf{F}(\mathbf{u}^{(1)})$ of equation (3.4) gives a expression for the nonlinear interaction of the fundamental partial bulk waves. This describes both self–interaction of each partial wave and cross–interaction between two different partial bulk waves. $\mathbf{F}(\mathbf{u}^{(1)})$ can be decomposed into driving forces for the longitudinal and transverse waves, respectively, which leads to the driving second harmonics $\mathbf{u}^{(\mathrm{DT})}_{\mathrm{T}m-\mathrm{L}n}$ $(m, n = 1, 2)$, $\mathbf{u}^{(\mathrm{DL})}_{\mathrm{L}m-\mathrm{L}m}$ $(m, n = 1, 2)$, $\mathbf{u}^{(\mathrm{DL})}_{\mathrm{T}m-\mathrm{T}m}$ $(m, n = 1, 2)$, $\mathbf{u}^{(\mathrm{DL})}_{\mathrm{T}m-\mathrm{L}n}$ $(m, n = 1, 2)$ and $\mathbf{u}^{(\mathrm{DL})}_{\mathrm{P1}-\mathrm{P2}}$ $(P = \mathrm{L}, \mathrm{T})$. The superscripts DL and DT denote the driven longitudinal and transverse components of these second harmonics. Since it is assumed that no dispersion is in the material of the waveguide, a cumulative effect taken place for the driven second harmonic $\mathbf{u}^{(\mathrm{DL})}_{\mathrm{L}m-\mathrm{L}m}$ $(m = 1, 2)$.

As shown in [29, 33], the solution is given as

$$\begin{aligned} \mathbf{u}^{(\mathrm{DL})}_{\mathrm{L}m-\mathrm{L}m} &= u^{(\mathrm{DL})}_{\mathrm{L}m-\mathrm{L}m} \left[\sin\theta_{\mathrm{L}} \frac{x_3}{h} + (-1)^{m-1} \cos\theta_{\mathrm{L}} \frac{x_2}{h} \right] \\ &\quad \times \mathbf{K}^0_{\mathrm{L}m} \exp[\imath 2 \mathbf{K}_{\mathrm{L}m} \cdot \mathbf{r}_m] \end{aligned} \tag{3.13}$$

where

$$
\begin{aligned}
u^{(\mathrm{DL})}_{\mathrm{L}m-\mathrm{L}m} &= \frac{\imath F^{(\mathrm{DL})}_{\mathrm{L}m-\mathrm{L}m}}{4K_{\mathrm{L}}(\lambda+\frac{4\mu}{3})}h \\
&= \frac{4\mu+3\lambda+2A+6B+2C}{4(\lambda+\frac{4\mu}{3})}\times\left(\frac{K_L}{k}\right)^2(kh)^2\left(\frac{u^2_{\mathrm{L}m}}{h}\right). \qquad (3.14)
\end{aligned}
$$

$F^{(\mathrm{DL})}_{\mathrm{L}m-\mathrm{L}m}$ represents the longitudinal driving force component and A, B and C are the third order elastic constants of the plate material. The displacement amplitude of the second harmonic is increasing with propagation distance, as $\mathbf{u}^{(\mathrm{DL})}_{\mathrm{L}m-\mathrm{L}m}$ is a linear function of the longitudinal coordinate x_3. Therefore $\mathbf{u}^{(\mathrm{DL})}_{\mathrm{L}m-\mathrm{L}m}$ accounts for the driven cumulative second harmonic. Additionally there is the driven second harmonic where no cumulative effect occur. It is termed as driven plane second harmonic.

The second harmonic must also satisfy the boundary condition of a stress free plate surfaces. This conditions can in general not be hold by the driven second harmonic only. As the driven second harmonic is just the particular solution of (3.4) the general solution can be find by stetting $\mathbf{F}(\mathbf{u}^{(1)}) = 0$. Because there is no driving force, the general solution of equation (3.4) is denoted as the freely propagating second harmonic. According to [11, 33] it is formulated as

$$
\begin{aligned}
\mathbf{u}^{(\mathrm{F})}_{\mathrm{L}m} &= \mathbf{u}^{(\mathrm{FC})}_{\mathrm{L}m}+\mathbf{u}^{(\mathrm{FP})}_{\mathrm{L}m} \\
&= \left\{\left[\cos\theta_{\mathrm{L}}\frac{x_3}{h}+(-1)^m\sin\theta_{\mathrm{L}}\frac{x_2}{h}\right]u^{(\mathrm{FC})}_{\mathrm{L}m}+u^{(\mathrm{FP})}_{\mathrm{L}m}\right\} \\
&\quad\times\mathbf{K}^0_{\mathrm{L}m}\exp[\imath 2\mathbf{K}_{\mathrm{L}m}\cdot\mathbf{r}_m] \qquad (3.15)
\end{aligned}
$$

and

$$
\begin{aligned}
\mathbf{u}^{(\mathrm{F})}_{\mathrm{T}m} &= \mathbf{u}^{(\mathrm{FC})}_{\mathrm{T}m}+\mathbf{u}^{(\mathrm{FP})}_{\mathrm{T}m} \\
&= \left\{\left[\cos\theta_{\mathrm{T}}\frac{x_3}{h}+(-1)^m\sin\theta_{\mathrm{T}}\frac{x_2}{h}\right]u^{(\mathrm{FC})}_{\mathrm{T}m}+u^{(\mathrm{FP})}_{\mathrm{T}m}\right\} \\
&\quad\times(-1)^{m-1}(\hat{x}_1\times\mathbf{K}^0_{\mathrm{T}m})\exp[\imath 2\mathbf{K}_{\mathrm{T}m}\cdot\mathbf{r}_m], \qquad (3.16)
\end{aligned}
$$

$m = 1, 2$ and $\mathbf{u}^{(\mathrm{F})}_{\mathrm{L}m}$ and $\mathbf{u}^{(\mathrm{F})}_{\mathrm{T}m}$ account for the freely propagating longitudinal and transverse second harmonics and $\mathbf{u}^{(\mathrm{FC})}_{Pm}$ ($P = \mathrm{L}, \mathrm{T}$) is the cumulative and $\mathbf{u}^{(\mathrm{FP})}_{Pm}$ ($P =$

L, T) the plane second harmonic.

The particular and general solution together gives the ultimate second harmonic of Lamb mode propagation, which satisfy the boundary condition:

$$\begin{aligned}\mathbf{u}^{(2)} &= \sum_{m=1}^{2}\big[\mathbf{u}^{(\mathrm{DL})}_{\mathrm{L}m-\mathrm{L}m}+\mathbf{u}^{(\mathrm{DL})}_{\mathrm{T}m-\mathrm{T}m}+\sum_{n=1}^{2}(\mathbf{u}^{(\mathrm{DL})}_{\mathrm{T}m-\mathrm{L}n}+\mathbf{u}^{(\mathrm{DT})}_{\mathrm{T}m-\mathrm{L}n})\\ &\quad +\mathbf{u}^{(\mathrm{F})}_{\mathrm{T}m}+\mathbf{u}^{(\mathrm{F})}_{\mathrm{L}m}\big]+\mathbf{u}^{(\mathrm{DL})}_{\mathrm{T1}-\mathrm{T2}}+\mathbf{u}^{(\mathrm{DL})}_{\mathrm{L1}-\mathrm{L2}}\ .\end{aligned} \tag{3.17}$$

Reducing the solution to its cumulative terms it becomes the ultimate cumulative second harmonic of Lamb mode propagation:

$$\mathbf{u}^{(\mathrm{2C})}=\sum_{m=1}^{2}\left[\mathbf{u}^{(\mathrm{DL})}_{\mathrm{L}m-\mathrm{L}m}+\mathbf{u}^{(\mathrm{FC})}_{\mathrm{T}m}+\mathbf{u}^{(\mathrm{FC})}_{\mathrm{L}m}\right]. \tag{3.18}$$

In solid materials the second harmonic stress comes from both $\mathbf{u}^{(2)}$ due to the linear Hooke's law and $\mathbf{u}^{(1)}$ from the nonlinear Hooke's law. The second harmonic boundary condition gives that

$$\begin{aligned}&\imath 2k[M(2\omega,2k)]\begin{bmatrix} u^{(\mathrm{FC})}_{\mathrm{L1}}\cos\theta_{\mathrm{L}}+u^{(\mathrm{DL})}_{\mathrm{L1}-\mathrm{L1}}\sin\theta_{\mathrm{L}}\\ u^{(\mathrm{FC})}_{\mathrm{T1}}\cos\theta_{\mathrm{T}}\\ u^{(\mathrm{FC})}_{\mathrm{L2}}\cos\theta_{\mathrm{L}}+u^{(\mathrm{DL})}_{\mathrm{L2}-\mathrm{L2}}\sin\theta_{\mathrm{L}}\\ u^{(\mathrm{FC})}_{\mathrm{T2}}\cos\theta_{\mathrm{T}}\end{bmatrix}\left(\frac{x_3}{h}\right)\\ &+\imath 2k[M(2\omega,2k)]\begin{bmatrix} u^{(\mathrm{FP})}_{\mathrm{L1}}\\ u^{(\mathrm{FP})}_{\mathrm{T1}}\\ u^{(\mathrm{FP})}_{\mathrm{L2}}\\ u^{(\mathrm{FP})}_{\mathrm{T2}}\end{bmatrix}=-\begin{bmatrix} T^{(2)}_{x_2x_3}(+h)\\ T^{(2)}_{x_2x_3}(-h)\\ T^{(2)}_{x_2x_2}(+h)\\ T^{(2)}_{x_2x_2}(-h)\end{bmatrix}\end{aligned} \tag{3.19}$$

where coefficient matrix $[M(2\omega,2k)]$ comes from the coefficient matrix $[M(\omega,k)]$ by applying $2kh$ for kh. In (3.19) the second term on the left hand side contains the parts of the driven plane second harmonic, the ultimate cumulative second harmonic and the four partial bulk waves.

To hold (3.19) on both boundaries,

$$[M(2\omega,2k)]\begin{bmatrix} u_{\mathrm{L1}}^{(\mathrm{FC})}\cos\theta_{\mathrm{L}}+u_{\mathrm{L1-L1}}^{(\mathrm{DL})}\sin\theta_{\mathrm{L}} \\ u_{\mathrm{T1}}^{(\mathrm{FC})}\cos\theta_{\mathrm{T}} \\ u_{\mathrm{L2}}^{(\mathrm{FC})}\cos\theta_{\mathrm{L}}+u_{\mathrm{L2-L2}}^{(\mathrm{DL})}\sin\theta_{\mathrm{L}} \\ u_{\mathrm{T2}}^{(\mathrm{FC})}\cos\theta_{\mathrm{T}} \end{bmatrix}=\mathbf{0} \tag{3.20}$$

and

$$\imath 2k[M(2\omega,2k)]\begin{bmatrix} u_{\mathrm{L1}}^{(\mathrm{FP})} \\ u_{\mathrm{T1}}^{(\mathrm{FP})} \\ u_{\mathrm{L2}}^{(\mathrm{FP})} \\ u_{\mathrm{T2}}^{(\mathrm{FP})} \end{bmatrix}=-\begin{bmatrix} T_{x_2x_3}^{(2)}(+h) \\ T_{x_2x_3}^{(2)}(-h) \\ T_{x_2x_2}^{(2)}(+h) \\ T_{x_2x_2}^{(2)}(-h) \end{bmatrix}. \tag{3.21}$$

must be satisfied. The condition $|M(\omega,k)|=0$ defines the dispersive equation of Lamb mode propagation (3.8)–(3.9), but in general the condition $|M(2\omega,2k)|=0$ can not get from $|M(\omega,k)|=0$. $|M(2\omega,2k)|\neq 0$ derive a trivial solution for (3.20). This leads to a second harmonic of Lamb mode propagation with no cumulative effect, where is not our focus on. So only for $|M(2\omega,2k)|=0$ cumulative second harmonic arise. $|M(2\omega,2k)|=0$ gives a nontrivial solution for (3.20) and from (3.21) it can be obtained that $u_{\mathrm{L1-L1}}^{(\mathrm{DL})}=u_{\mathrm{L2-L2}}^{(\mathrm{DL})}$ holds for $u_{P1}=u_{P2}$ as well as $u_{P1}=-u_{P2}$ ($P=\mathrm{L},\mathrm{T}$). This shows that only the symmetric second harmonic of Lamb mode propagation is cumulative.

Take the condition $|M(2\omega,2k)|=0$ yields to

$$\begin{aligned} u_{\mathrm{L1}}^{(\mathrm{FC})}\cos\theta_{\mathrm{L}}+u_{\mathrm{L1-L1}}^{(\mathrm{DL})}\sin\theta_{\mathrm{L}} &= u_{\mathrm{L2}}^{(\mathrm{FC})}\cos\theta_{\mathrm{L}}+u_{\mathrm{L2-L2}}^{(\mathrm{DL})}\sin\theta_{\mathrm{L}}, \\ u_{\mathrm{T1}}^{(\mathrm{FC})}\cos\theta_{\mathrm{T}} &= -u_{\mathrm{T2}}^{(\mathrm{FC})}\cos\theta_{\mathrm{T}}, \end{aligned} \tag{3.22}$$

$$\begin{aligned} u_{\mathrm{L1}}^{(\mathrm{FC})}\cos\theta_{\mathrm{L}}+u_{\mathrm{L1-L1}}^{(\mathrm{DL})}\sin\theta_{\mathrm{L}} &= -u_{\mathrm{L2}}^{(\mathrm{FC})}\cos\theta_{\mathrm{L}}-u_{\mathrm{L2-L2}}^{(\mathrm{DL})}\sin\theta_{\mathrm{L}}, \\ u_{\mathrm{T1}}^{(\mathrm{FC})}\cos\theta_{\mathrm{T}} &= u_{\mathrm{T2}}^{(\mathrm{FC})}\cos\theta_{\mathrm{T}}. \end{aligned} \tag{3.23}$$

From (3.22) and (3.23) we can see that the ultimate cumulative second harmonic can be symmetric or antisymmetric. But the driven and freely propagating second

harmonics should have the same symmetry characteristics. The freely propagating second harmonic have to be symmetric due to term $u^{(\mathrm{DL})}_{\mathrm{L1-L1}} = u^{(\mathrm{DL})}_{\mathrm{L2-L2}}$. Therefore, the ultimate cumulative second harmonic $\mathbf{u}^{(2)}$ must be symmetric.

This condition for the cumulative second harmonic generation must be considered by the choice of the excitation setpoints, which will be described later.

3.2 Existence condition for the cumulative second harmonic field

As shown, $|M(\omega, k)| = 0$ mostly not lead that $|M(2\omega, 2k)| = 0$. But for the generation of cumulative second harmonic $|M(\omega, k)| = 0$ and $|M(2\omega, 2k)| = 0$ must be satisfied simultaneous. As the ultimate cumulative second harmonic $\mathbf{u}^{(2\mathrm{C})}$ is symmetric, the symmetric term (3.8) of the dispersion equation must be considered:

$$\frac{\tan(\alpha_{\mathrm{T}} 2kh)}{\tan(\alpha_{\mathrm{L}} 2kh)} = -\frac{4\alpha_{\mathrm{T}}\alpha_{\mathrm{L}}}{\left(2 - \frac{c_{\mathrm{ph}}^2}{c_{\mathrm{T}}^2}\right)^2} \tag{3.24}$$

Combine this equation with the one of the dispersion equations of Lamb mode propagation (3.8) or (3.9) gives

$$\tan(\alpha_{\mathrm{T}} kh) = \tan(\alpha_{\mathrm{L}} kh), \tag{3.25}$$

or more simplified

$$\alpha_{\mathrm{T}} kh = \alpha_{\mathrm{L}} kh + n\pi \quad n \in \mathbb{N}. \tag{3.26}$$

Replacing α_{T} and α_{L} by the expressions of (3.6) leads to

$$kh = \frac{n\pi}{\left(\sqrt{\left(\frac{c_{\mathrm{ph}}^2}{c_{\mathrm{T}}^2}\right)^2 - 1} - \sqrt{\left(\frac{c_{\mathrm{ph}}^2}{c_{\mathrm{L}}^2}\right)^2 - 1}\right)}, \quad c_{\mathrm{ph}} \neq c_{\mathrm{L}}, c_{\mathrm{T}}. \tag{3.27}$$

By combine equation (3.8) and (3.27) or equation (3.9) and (3.27) the existence conditions $|M(\omega, k)| = |M(2\omega, 2k)| = 0$ for cumulative second harmonics can be achieved. A numerical solution can be computed [12]. From the numerical solution

the condition for cumulative second harmonics is derived. The phase velocities of the exciting mode at the fundamental frequency and the excited mode at the second harmonic frequency have to be equal.
In conjunction, following conditions has to be satisfied that generation of cumulative second harmonic occur:

- The excited mode of the second harmonic frequency has to be symmetric, that a cumulative effect for a propagating Lamb wave exist
- The phase velocities of exciting fundamental frequency mode and excited second harmonic frequency mode must be equal.

With this defined conditions for cumulative second harmonics an excitation setpoints for cumulative second harmonic generation can be found. A cumulative second harmonic excitation setpoint accounts for two points on two different symmetric modes, which have the same phase velocity for fundamental and second harmonic frequency (see Figure 3.1). In this work the setpoint for the symmetric mode pair s1 $\rightarrow$ s2 is chosen, like in Bermes work [3]. This excitation setpoint has the advantage compared to other setpoints, that the modes s1 and s2 are "forerunner" and therefore not influenced by other modes as shown in Figure 3.2 , the in time-frequency domain representation of the mode curves. The numerical values for the s1 $\rightarrow$ s2 pairs are 3.5685 MHz for the fundamental frequency f_1, 7.1370 MHz for the second harmonic frequency f_2 and a phase velocity c_{ph} of 6349.0 $\frac{m}{s}$. The values are based on the determined dispersion curves, which are computed for a normalized frequency $\frac{f}{h}$. h stays for the plate thickness, which is chose here with 1 mm. If the plate thickness differs, the frequency of the fundamental and second harmonic must be divided by the plate thickness.

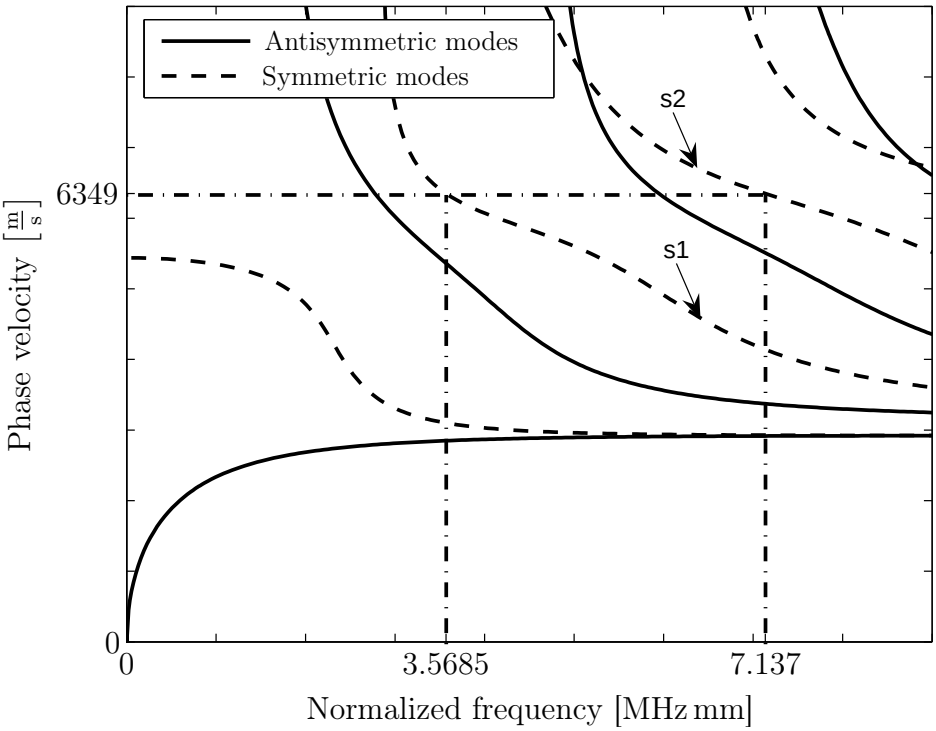

Figure 3.1: Cumulative second harmonic excitation setpoint s1 → s2.

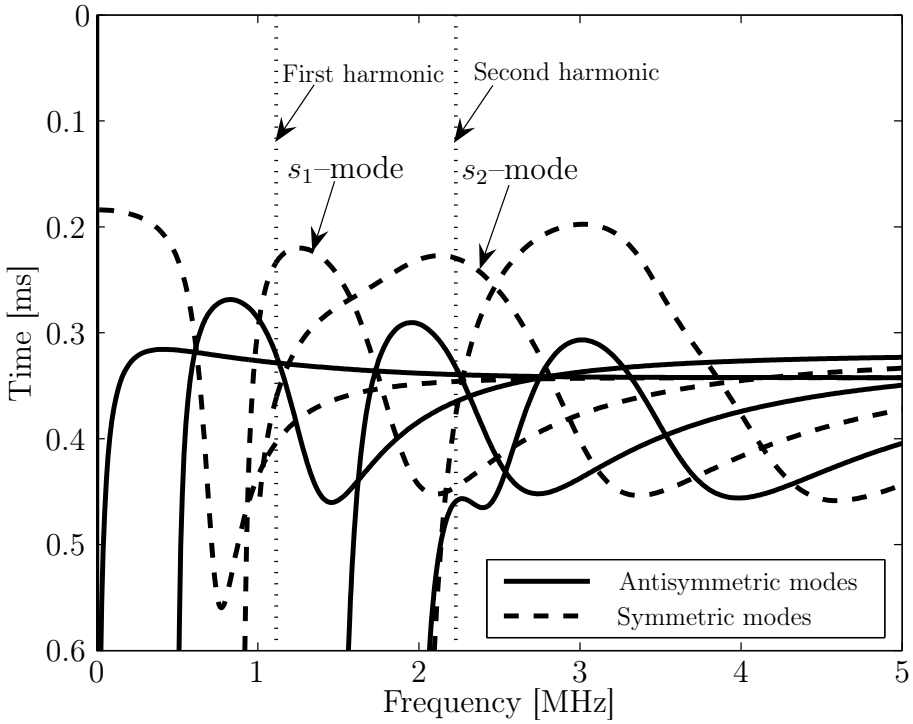

Figure 3.2: Mode–curves in time–frequency domain

CHAPTER IV

EXPERIMENTAL PROCEDURE

In this section the experimental procedure is explained. The experimental setup can be divided into two parts. First, the generation side of a Lamb wave in the wave guide. Second, the detection side to measure the out–of–plane velocity a point on the surface of the plate caused by the propagating Lamb wave. Also an exact description of the used specimens will be given.

Foremost a overview of the complete experimental setup is represented.

4.1 Experimental setup

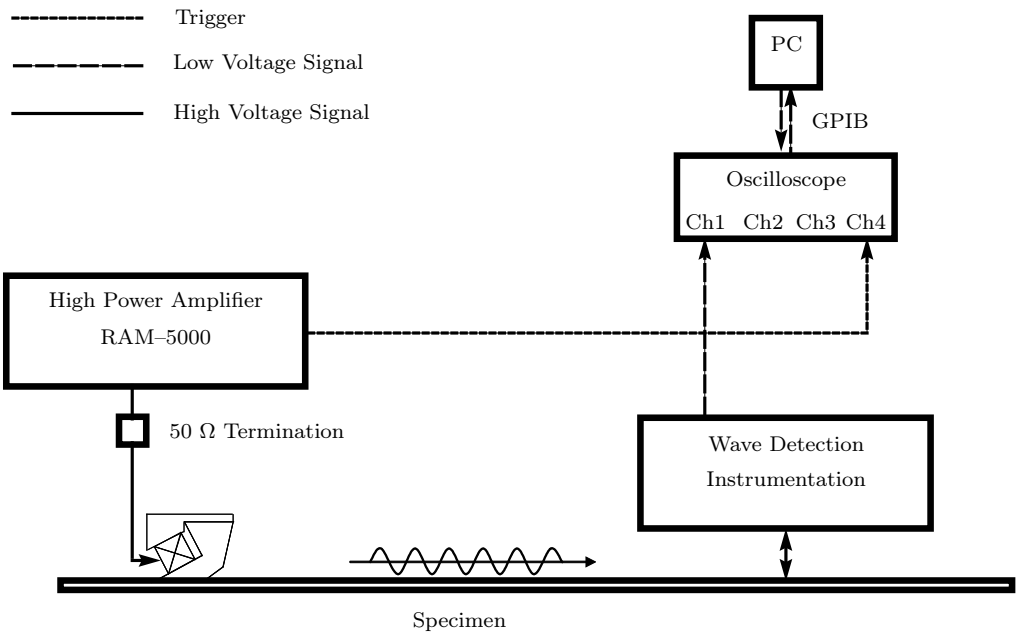

Figure 4.1: Experimental setup.

In Figure 4.1 the complete setup is illustrated. For the generation of the Lamb wave a high power amplifier RITEC RAM–5000 Mark IV is used to create a high

voltage toneburst signal of a frequency of 2.225 MHz. No extra waves generator is necessary hence the RAM–5000 has an internal wave generator. As shown in [3], [21] the input voltage level for the excitation transducer has no influence on the nonlinearity value A_2/A_1^2. Therefore the maximum output level of the amplifier with 1280 V is chosen to get the biggest wave displacement amplitude. The cycle length is 25 to get a long enough steady–state part of the output signal. This waveform signal is led in a narrow band ultrasonic transducer PANAMETRICS X1055 (lead zirconate titanate) with a center frequency $f_{\text{center}} = 2.25\,\text{MHz}$. The transducer is coupled with oil on a plexiglas wedge. The wedge is than also coupled with oil and fixed on the specimen thin metal sheet specimen. For the detection of the propagating wave two different instruments were used: a laser interferometer system and the detection with a wedge and transducer. They will be explained in detail and compared later. The detection system gives a voltage signal proportional to the displacement of the specimen. The noise level of the signal has to be as small as possible since the amplitude of the second harmonic is very low. For this reason, the voltage signal is filtered by a low pass filter with an edge frequency of 20.4 MHz to reduce the noise level and than been sent in to a second Tektronix TDS 420 oscilloscope. For the detection of the relative weak second harmonic the noise of the signal has to be as small as possible. To get a higher signal–to–noise ratio a average of repeated measurements is computed with the oscilloscope. Since the noise is random, it will be canceled out with the averaging the signal. The average of 1000 measurements is made in the measurements, which gives adequate noise reduction [20]. The oscilloscope discretized the signal with a sampling frequency of 25 MHz and 15000 sample points. The digital signal is than transfered with a General Purpose Interface Bus (GPIB) connection from the oscilloscope to a PC. The PC is used to process the signal. The signal processing is explained in a later section. The internal trigger signal of the RAM–5000 amplifier is used as trigger signal of the complete setup.

4.2 Generation of Lamb waves in wave guides

Several methods are known for inducing a Lamb wave. Theres is the generation with a pulsing laser source, electromagnetic acoustic transducers (EMATs), the comb transducer technique or the angle beam excitation [28], also termed as wedge method. The wedge method is often used to create surface waves in waveguides [3, 16, 20] and is also applied in this research. The wedge method itself, the requirements and design of the wedge will be explained in the following section.

4.2.1 Wedge method

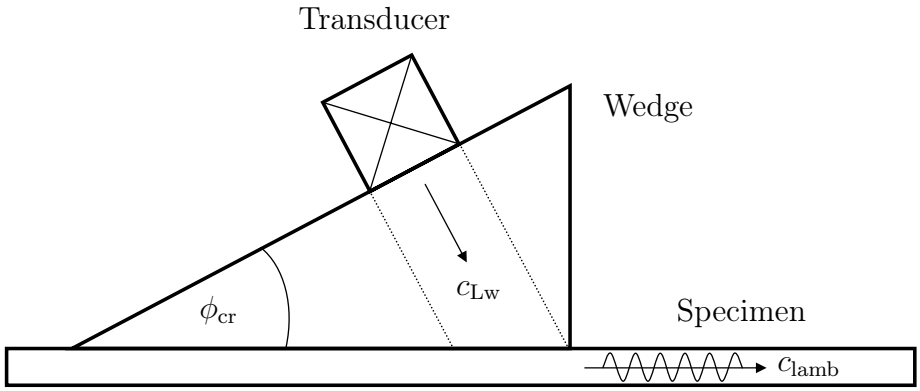

Figure 4.2: Generation of a Lamb wave with the wedge method.

The setup of the wedge method is illustrated in Figure 4.2. The ultrasonic transducer is coupled to the wedge. The wedge itself is again coupled on the waveguide. To avoid to strong reflections on the transitions transducer–wedge and wedge–waveguide, oil is used as acoustic coupling. The piezoelectric transducer is bounded on the sloping surface of the wedge. So the from transducer generated longitudinal waves propagates through the wedge and hits the wave guide surface in the critical angle ϕ_{cr}. To induce a Lamb wave, the angle has to meet the surface wave excitation condition. The correct angle can be defined with the Snell's law (Figure 4.3).

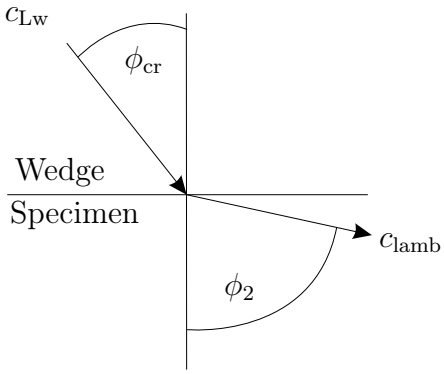

Figure 4.3: Snell's law for angle beam analysis.

$$\sin(\phi_2)\, c_{\mathrm{Lw}} = \sin(\phi_{\mathrm{cr}})\, c_{\mathrm{lamb}}, \tag{4.1}$$

where c_{lamb} is the phase velocity of the chosen cumulative second harmonic excitation setpoint, c_{Lw} the longitudinal wave speed of the wedge material, ϕ_1 the incident and ϕ_2 the refraction angle. To generate a surface wave the angle ϕ_2 has to be $\phi_2 = 90°$ or $sin\phi_2 = 1$. So from equation (4.1) the critical angle ϕ_{cr} of wedge is given as

$$\phi_{\mathrm{cr}} = \arcsin\left(\frac{c_{\mathrm{Lw}}}{c_{\mathrm{lamb}}}\right). \tag{4.2}$$

Due to the argument of the arcsin must be ≤ 1 it follows that the longitudinal wave speed of the wedge material has to be equal or less than the the phase speed of the Lamb wave. To satisfy this condition the material of the wedge should have small longitudinal wave velocity for example plastic.

Compared to other excitation methods, the wedge method sends all the energy in one single wave mode and in one particular direction. For this work it has the advantages that the cumulative second harmonic can be better observed and the amplitudes of the wave displacements are bigger. If a more broadband frequency spectrum is needed an excitation with a laser is a more proper choice.

4.2.2 Wedge design

To excite a Lamb wave with high partial motion amplitude as possible, several energy losses from the transducer to the actual wave guide has to be taken into account. Bermes [4] and Herrmann [21] examined different influences and improved the wedge design. There is the effect of beam divergence or also called ultrasonic diffraction. The ultrasonic transducer can not launch a perfect plane longitudinal wave. Diffraction occurs and so not the complete beam from the transducer hits the interface between wedge and specimen in the critical angle. The beam components, which hit the interface not the critical angle will not excite the wanted Lamb wave mode. Instead bulk waves or other Lamb wave modes are generated. This results in an loss of energy for the excitation of the right Lamb wave mode and so in a smaller motion amplitude. To reduce this effect the propagation distance in the wedge should be as short as possible.

Further there is attenuation in the wedge material. As mention before the phase velocity of the wedge must be smaller as the phase velocity of the wave guide to fulfill the excitation condition. So plastic is a good choice. The disadvantage is, that plastic has a relatively high attenuation. Hence, there is a decrease of the signal strength due to the attenuation. The attenuation coefficient is defended as decibel per millimeter. This leads to the same criteria, that the propagation distance in the wedge between transducer and specimen should be as short as possible. According to Ginzel [17] polystyrene and plexiglass have a low attenuation coefficient and so are proper materials. To compare the two different wedge materials, two items have to be considered. First the attenuation coefficient of the material at the first harmonic frequency $f = 2.225$ MHz. With the propagation distance we can calculate the damping D. But additional the critical angle is changing due to the different phase velocities of the wedge materials. So the propagation distance is also changing.

The critical angle can be computed with the Snell‘s law as described before. The

longitudinal wave speed at the frequency $f = 2.225$ MHz for polystyrene is $c_{\mathrm{Lw,po}} = 1960\,\frac{\mathrm{m}}{\mathrm{s}}$ and plexiglass is $c_{\mathrm{Lw,pl}} = 2751\,\frac{\mathrm{m}}{\mathrm{s}}$ [20]. The Lamb phase velocity for the chosen aluminum 1100-H14 is $c_{\mathrm{lamb}} = 6349\,\frac{\mathrm{m}}{\mathrm{s}}$. So the critical angle for the cumulative second harmonic excitation s_1 for the two materials is

$$\phi_{\mathrm{cr,po}} = \arcsin\left(\frac{c_{\mathrm{Lw,po}}}{c_{\mathrm{lamb}}}\right) = \arcsin\left(\frac{1960\,\frac{\mathrm{m}}{\mathrm{s}}}{6349\,\frac{\mathrm{m}}{\mathrm{s}}}\right) = 17.98° \tag{4.3}$$

$$\phi_{\mathrm{cr,pl}} = \arcsin\left(\frac{c_{\mathrm{Lw,pl}}}{c_{\mathrm{lamb}}}\right) = \arcsin\left(\frac{2751\,\frac{\mathrm{m}}{\mathrm{s}}}{6349\,\frac{\mathrm{m}}{\mathrm{s}}}\right) = 25.68°. \tag{4.4}$$

The propagation distance can be derived by (see Figure 4.4)

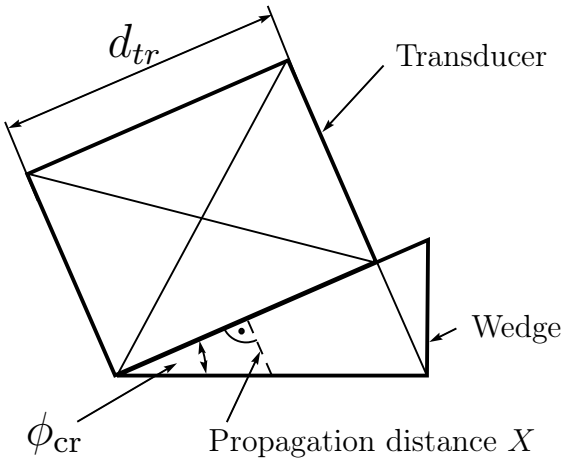

Figure 4.4: Propagation distance in the wedge

$$X_{\mathrm{po}} = \frac{d_{\mathrm{tr}}}{2} * \tan\left(\phi_{\mathrm{cr,po}}\right) = \frac{16mm}{2} * \tan\left(17.98°\right) = 2.60mm \tag{4.5}$$

$$X_{\mathrm{pl}} = \frac{d_{\mathrm{tr}}}{2} * \tan\left(\phi_{\mathrm{cr,pl}}\right) = \frac{16mm}{2} * \tan\left(25.68°\right) = 3.85mm. \tag{4.6}$$

The attenuation coefficient at the first harmonic frequency $f = 2.225$ MHz is for polystyrene $\approx 0.18\frac{\mathrm{dB}}{\mathrm{mm}}$ and for plexiglas $\approx 0.6\frac{\mathrm{dB}}{\mathrm{mm}}$. So the damping D results as

$$D_{\mathrm{po}} = X_{\mathrm{tr}} * 0.60\frac{\mathrm{dB}}{\mathrm{mm}} = 2.60mm * 0.60\frac{\mathrm{dB}}{\mathrm{mm}} = 1.60dB \tag{4.7}$$

$$D_{\mathrm{pl}} = X_{\mathrm{tr}} * 0.18\frac{\mathrm{dB}}{\mathrm{mm}} = 3.85mm * 0.18\frac{\mathrm{dB}}{\mathrm{mm}} = 0.69dB. \tag{4.8}$$

It polystyrene would be used as wedge material the attenuation of the wave in the wedge would be almost double so high. Therefore plexiglas is taken in the experiments as wedge material.

To get the shortest possible propagation distance for the longitudinal wave, the wedge design of Bermes [3] can be improved as shown in Figures 4.5 and 4.6. So the base

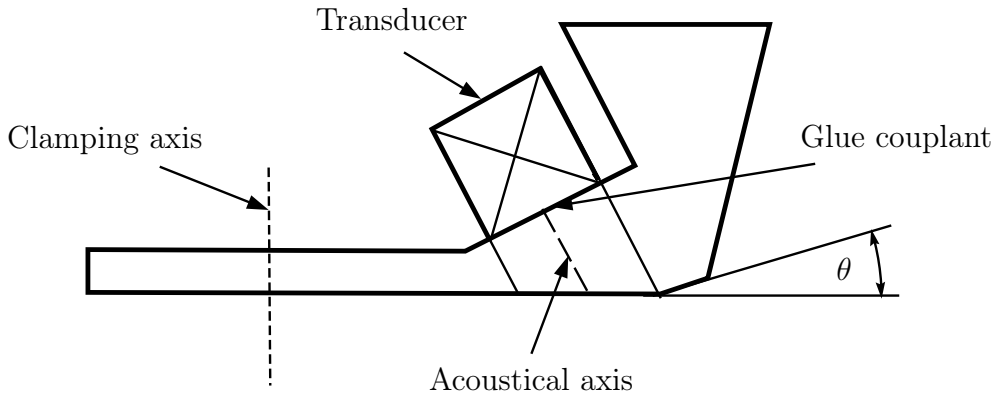

Figure 4.5: Old wedge design

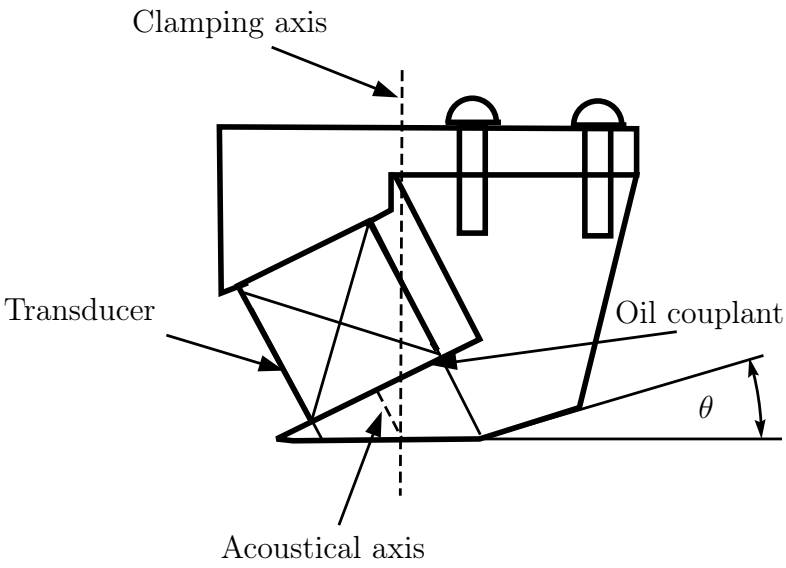

Figure 4.6: Improved wedge design

of the wedge has been removed. The top of the wedge is now used as the clamping surface. This also has the advantage that the clamping axis is in the middle of wedge–specimen interface, which guarantees better contact. The voluminous part above the incline θ acts as the attenuation area. The reflected waves from the wedge–specimen interface are reflected, so that as less as possible comes back to the interface and excites other, unwanted waves. Air and solid have very different acoustic impedances. On air–solid–interfaces, most of the wave energy is reflected and not transmitted. So only a small amount of energy from the excited wave is transmitted in the next body through the gaps between the transducer–wedge and wedge–specimen interfaces.
A thin film of oil, glycerin, water or glue is placed in the gap to significantly reduce the impedance mismatch. Both used glue as coupling between the transducer and the wedge and oil between wedge and specimen. In Herrmann‘s [20] work the coupling glue and oil are compared. Oil gives much better coupling material than glue, because in glue pattern and even air bubble can be found in the glue after hardening. It could also be observed, that the glue corrodes the plexiglas. If the transducer has been removed and glued anew, the surface of the wedge was no longer even and the coupling quality declined. This manifested itself as attenuation in excited wave. A clamping fixture for the transducer on the wedge has been developed as illustrated in Figure 4.6, so oil-coupling is possible. This improvement of the wedge design gives a significant increase in the generated first harmonic wave amplitude as shown in Figure 4.7.

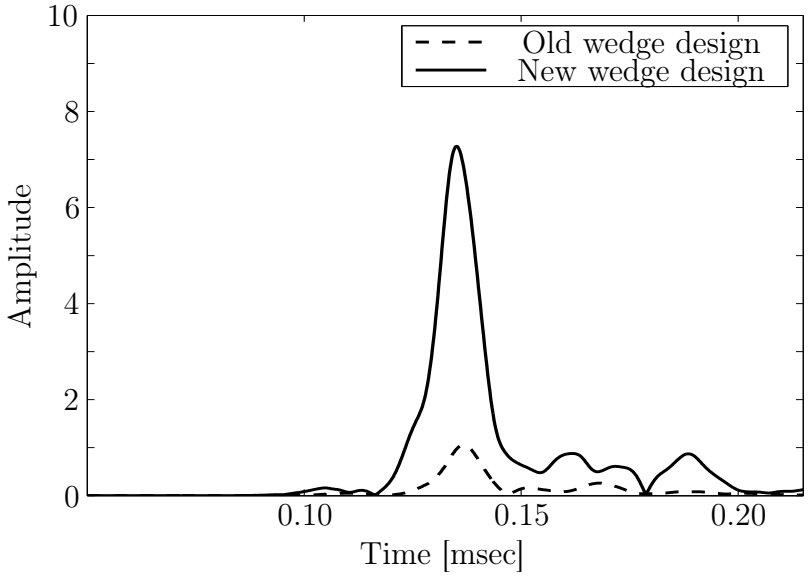

Figure 4.7: Amplitude of the fundamental wave

4.3 Wave detection instrumentation

Two different methods are used to detect the out–of–plane motion of the specimen caused by the propagation Lamb wave.

4.3.1 Single probe heterodyne laser interferometer

Figure(4.8) shows the complete laser interferometer system as used from Herrman [20] and Bermes [3]. A laser measurement system is a broadband and highly sensitive detection system. With the Doppler effect, the absolute particle velocity is determined. The particle velocity amplitude is proportional to the displacement amplitude, which we want to detect. The laser beam is produced by a 2 Watt Argon Laser. The single beam has a wavelength of 514.4 nm and is vertically polarized. To split the beam in a object and reference beam a acousto–optic modulator (AOM) is used. AOM consists of an activated piezocrystal. This crystal splits the incoming laser beam in a infinite number of separate beams. But the zero–and first–order beam together already carry already approximately 95 %. This two are taken as objective and reference beam. The first–order beam is addionally frequency shifted by $f_b = 40\,\mathrm{MHz}$ due to the beat

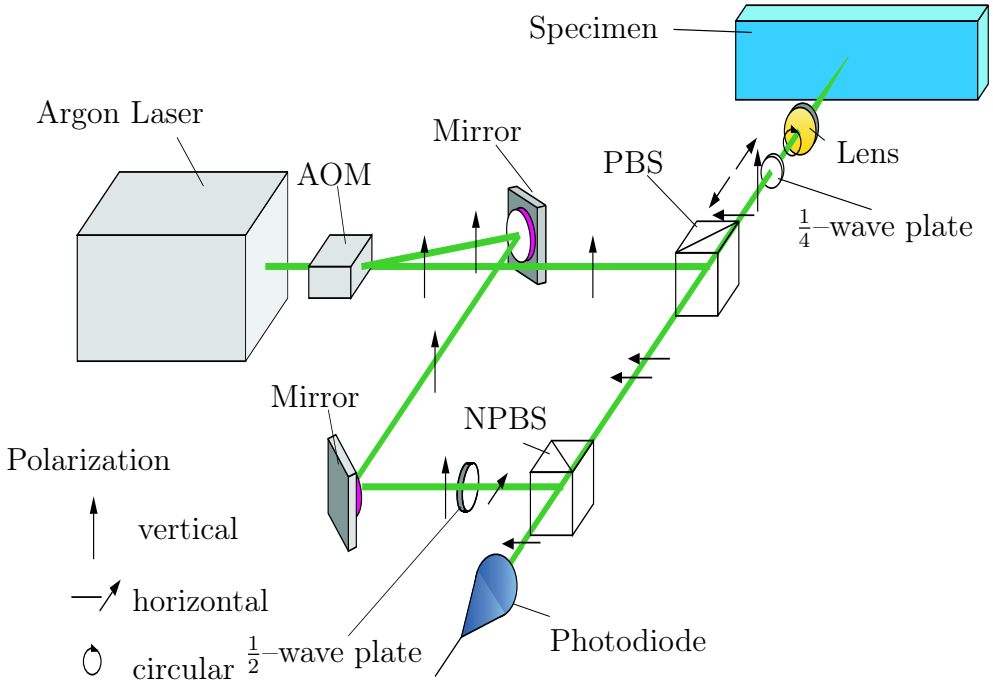

Figure 4.8: Laser interferometer detection system.

frequency of the piezocrystal. The unshifted object beam is sent in a ploarized beam splitter (PBS). The PBS let horizontally polarized light pass and reflect vertical polarized light. The beam is defleced to the specimen, focused by a lense and reflected back from the specimen surface to the PBS. On the way to the specimen and back to the PBS the beam passes two times a $\frac{1}{4}$–wave plate. This rotate the beam about 90°. So the beam is now horisontal polarized and pass the PBS. The beam goes in nonpolarzed beam splitter (NPBS). The object beam recombine in the NPBS with the from mirrors deflected and from a $\frac{1}{2}$–wave plate rotated reference beam. If there is no out–of–plane velocity of the specimen surface the recombined laser beam has the same frequency f as the orginal laser signal, but is modulated with the AOM frequency $f_b = 40\,\mathrm{MHz}$. When a out–of–plane velocity is generated by the propagating wave the object beam will be shift again. This is called Doppler shift. The frequency shifted can be calculated with

$$\Delta f = \frac{2fv}{c}, \tag{4.9}$$

with v is the out–of–plane surface velocity of the specimen, f is the original frequency of the object beam, and c stays for the speed of light. So the modulation frequency of the combined beam changes. The laser beam is than detected by a photo diode. The photo diode converts the light intensity changes due to the modulation in a voltage signal. The signal is feed in a FM discriminator. The FM discriminator transform the frequency shift of the input signal in output voltage signal proportional to the frequency shift. This signal is proportional to the out–of–plane velocity of the specimen and is sent it a oscilloscope to monitor and discretized it.

4.3.2 Wedge method

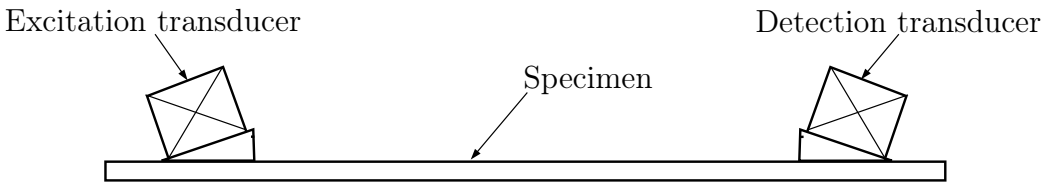

Figure 4.9: Wave detection with wedge-transducer combination

A other technique to detect the out–of–plate motion of the specimen surface is to use a wedge–transducer combination such as for the generation the Lamb wave (Figure 4.9). The wave is converted in a longitudinal wave, travels through the wedge and deformate the transducer. The transducer gives a voltage output signal due to the piezoelectric effect. Because the amplitude of the second harmonic is relatively low compared to the fundamental harmonic amplitude, a narrow band ultrasonic transducer PANAMETRICS A109S with a center frequency of $f_{\text{center}} = 5\,\text{MHz}$ is taken for the receiving side. So the second harmonic components with a frequency of 4.45 MHz will be better detected.

4.3.3 Comparison of the laser interferometer and the wedge–transducer method

Both the laser interferometer and the wedge–transducer techniques have advantages and disadvantages. As mentioned the laser is a broadband measurement system. Additionally the out–of–plane velocity of the specimen can be measured non–contact and without mechanical resonance of the transducer. So the amplitudes of the first and second harmonic are absolutely measured in a resonance free ratio. If the absolute parameter β needs to be determined, the laser interferometer has to be used. But if the absolute value of β is not critical, as in this work, a relative nonlinearity value A_2/A_1^2 can be determined.

For the detection with a wedge detection method, a transducer with a center frequency of $f_{\text{center}} = 5\,\text{MHz}$ been chosen. So the weaker second harmonic wave is measured in a relatively more sensitive fashion. Even with the wedge generation method, not only one single mode is excited; there are other modes launched. Since the detection wedge must also satisfy the critical angle condition, the modes s_1 and s_2 are detected in a more sensitive fashion. This behavior can be observed in the plots of the first and second harmonic frequency as a function of time of a detected Lamb wave signal (Figures 4.10 and 4.11). The time–domain representation for a certain frequency can be obtained with a short–time Fourier transformation (STFT), which is explained in detail later in this chapter.

The laser measures at one single point with high resolution. For fundamental research of the wave field in detail, a raster–scanning of the specimen with a laser can be performed[5]. The result is a image with high resolution of the displacement field. The wedge gives the average of the wave motion over an area. For the narrow specimens which are used in this study the average over a area from the wedge has a advantage. The edge reflections from the sides of the specimen give a distinct modulation structure [5]. Since the structures are not equal for the fundamental

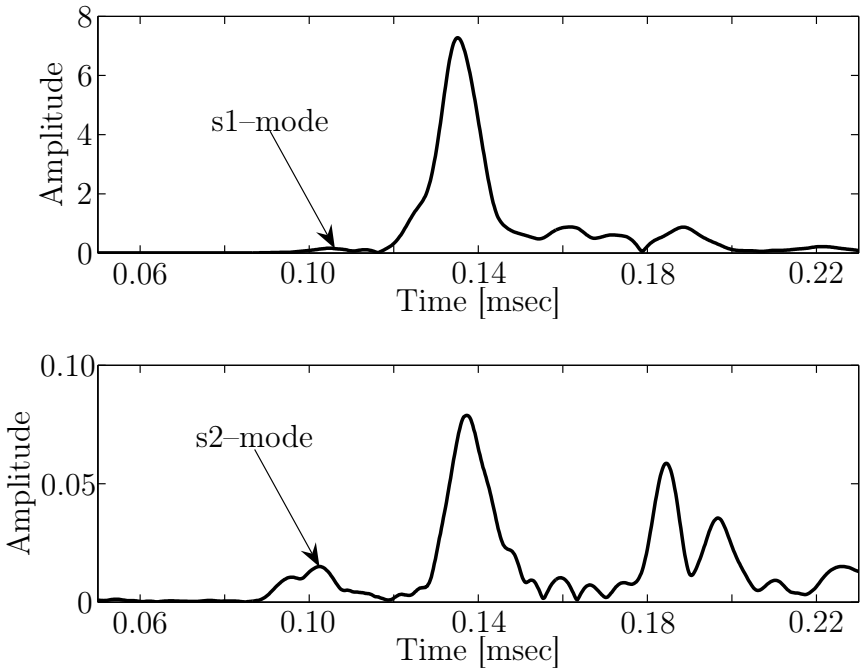

Figure 4.10: Fundamental and second harmonic frequency as functions of time detected with the laser interferometer.

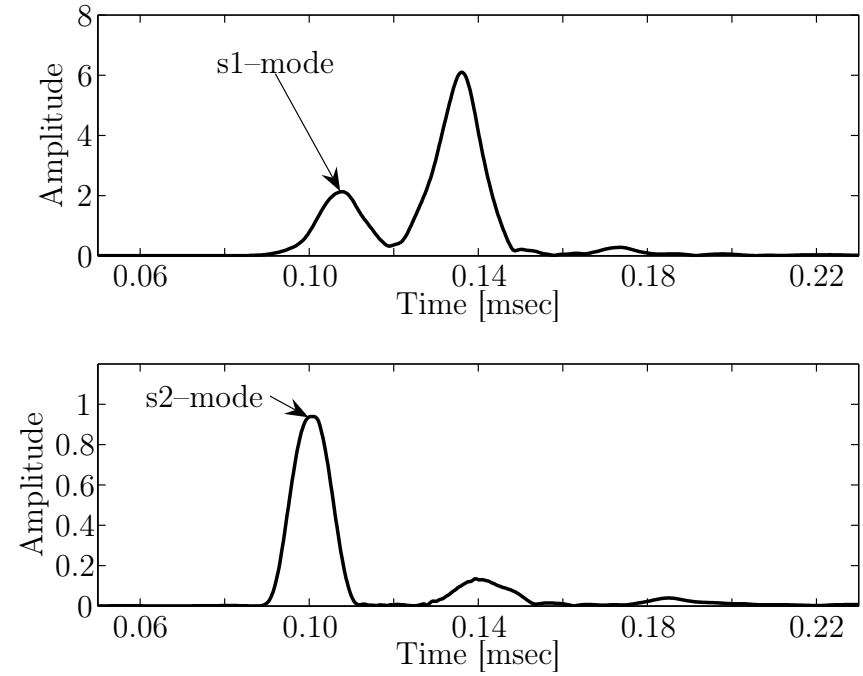

Figure 4.11: Fundamental and second harmonic frequency as functions of time detected with the wedge method.

and second harmonics, the determined nonlinearity value A_2/A_1^2 is dependent on the measurement point. This can be avoided when a wedge and a transducer is used for the measurement. To avoid the influence poor coupling between the wedge and the specimen, the average of three measurements is been taken and every time the wedge is completely removed an re–coupled between the measurements. For the application in the field, the laser system has the drawback of being sensitive to vibrations. For a laser measurements the surface has to be highly reflective, so sometimes polishing is necessary. On the other hand to coupling the wedge to the specimen, the specimen has to be even, which is not the case for the laser measurement. Both the laser interferometer and the wedge method are applied in the experiments and the measurement results are compared.

4.4 Specimens

The specimens which are used to detect the effect of change the of microstructure on the nonlinearity parameter is shown in Figure 4.12. The specimen is made as long

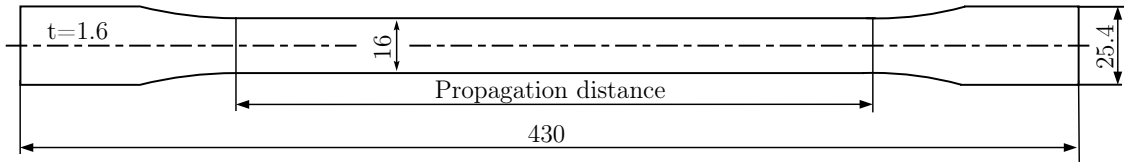

Figure 4.12: Specimens (all measures in mm)

as possible. The longer the specimen the better is the nonlinearity parameter change is measurable and also the modes are better separated in the time domain. But the length of the specimen was limited by the clamping length in the load frame for the load tests. The material is a aluminum 1100-H14. The thickness has to be chosen so that fundamental frequency for the excitation of the s_1–mode comes close as possible to the center frequency of $f_{\text{center}} = 2.25\,\text{MHz}$ of the wave generation transducer. The fundamental frequency is $f_1 = 3.5685\,\text{MHz}$ mm. This leads to the optimal plate

thickness of

$$d_{\text{opt}} = \frac{f_1}{f_{\text{center}}} = \frac{3.5685\,\text{MHz mm}}{2.25\,\text{MHz}} = 1.586\,\text{mm}. \tag{4.10}$$

As Bermes [4] a aluminum plate with thickness of $d = 1.6\,\text{mm}$ is chosen so that the excitation frequency is shifted to $f = 2.23\,\text{MHz}$. In this work a frequency of $f = 2.225\,\text{MHz}$ is taken for the wave generation in the experiments. The frequency is close to the center frequency of the transducer $f_{\text{center}} = 2.25\,\text{MHz}$, which gives a large oscillation amplitude of the transducer.

4.5 Signal processing

Detecting the material nonlinearity and the increase with change of microstructure in metals is very difficult. The Lamb wave has a dispersive and multimode characteristic. Every mode travels with a different group velocity and therefore each mode arrives at a different time. But for short propagation distance, the modes not separate clear from each other (see Figure 4.13). The signal processing of the signal from the detection unit is a crucial factor to separate the modes.

No really steady state parts for every mode can be observed. So the single time window and fast Fourier transformation is not a sufficient technique since the single modes can not right identified. To be sure to extract the right amplitudes for the first harmonic A_1 and second harmonic A_2 a representation of the signal in a time–frequency representation is necessary. There are different methods to get the time–frequency representations of the signal [3]. In this work the short–time Fourier transformation (STFT) is taken to get a time–frequency representation of the time–domain signal. With a illustration in time–frequency the arriving time of the different modes for certain frequencies can be determined. So is secure that the right peaks for the amplitudes A_1 and A_2 for the first and second harmonic are picked. Also can be seen if the modes influencing each other because even if the wedge method should launch only the s_1–mode, several modes are exited.

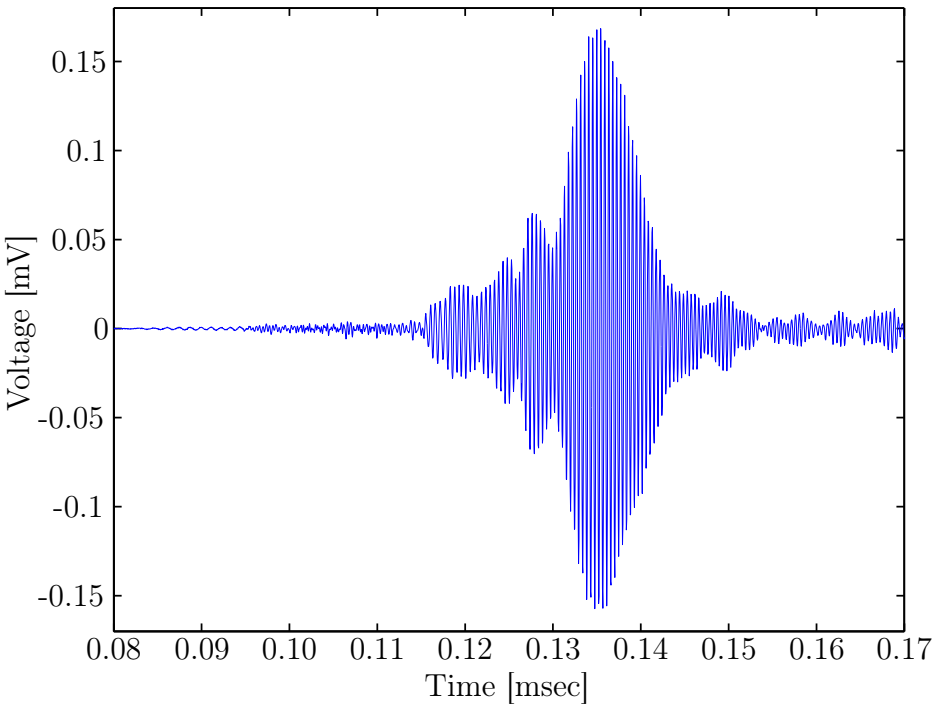

Figure 4.13: Typical time signal with overlapping Lamb modes.

A short instruction of the short–time Fourier transformation will provided. The discrete Fourier transformation is defined as

$$s[n] = \int_0^{2\pi} S(\omega) e^{\imath\omega n} \mathrm{d}\omega \tag{4.11}$$

with

$$S(\omega) = \frac{1}{2\pi} \sum_{n=-\infty}^{\infty} s[n] e^{-\imath\omega n} \tag{4.12}$$

$S(\omega)$ is the Fourier transformation of discrete signal $s(n)$. The frequency f is referred to the angular frequency ω by the equation

$$\omega = 2\pi f. \tag{4.13}$$

The values of the Fourier transformation $S(\omega)$ are usually complex. A common way is to calculate the energy density spectrum

$$E_\mathrm{d} = |S(\omega)|^2. \tag{4.14}$$

This gives the energy distribution over the frequency. To get in addition the information which frequency appears at which time a time–frequency analysis is required. For example a short–time Fourier transformation (STFT)

$$S_{\mathrm{stft}}(\omega, t) = \frac{1}{2\pi} \int_{-\infty}^{\infty} e^{-\imath\omega\tau} s(\tau) h(\tau - t) \mathrm{d}\tau, \tag{4.15}$$

$h(t)$ is the window function of the Fourier transformation. The complete discrete time–domain signal in fractioned by the window function in small overlapping parts. Each part represent a small time window and Fourier transformed separated. Thus it can be detect which frequency is how strong present at a certain time. The energy density spectrum of the STFT is calculated identical as for the Fourier transformation

$$E_{\mathrm{d}}(\omega, t) = |S_{\mathrm{stft}}(\omega, t)|^2. \tag{4.16}$$

A plot of the energy density spectrum over frequency and time is called energy spectrogram. This is used for the analysis of the measurement signal in this work. It should be mentioned that the sampling frequency for the continuous time signal should be at least double so high as the frequency what will be observed. In the experiments the highest frequency is the second harmonic with 4.3 MHz. So the sampling frequency should be at least 8.6 MHz. Therefore the chosen sampling frequency in the experiments of 25 MHz is high enough. A example of a spectrogram of a Lamb wave from the experiments is given in the Figure 4.14. The lines in the spectrogram are the theoretical disperse curves and obtained from the group velocity representation in the frequency domain. We can see, that it is not possible to excite only one single mode even with the wedge method. But the theoretical curves a clear mode identification is feasible. The wave amplitudes parallel to the theoretical wave mode curves are the reflection of the Lamb wave on the side edges of the specimen. For the computation of the relative nonlinearity value A_2/A_1^2 the amplitude of $s1$–mode at the fundamental frequency and amplitude of the $s2$–mode at the second harmonic frequency has

to be identified. The horizontal lines in the spectrogram mark the fundamental and second harmonic frequency. Peaks of the energy density for the $s1$–mode (A_1) and the $s2$–mode (A_2) can be found close to the theoretical curves. Figure 4.15 shows the cuts of spectrogram at the according frequencies.

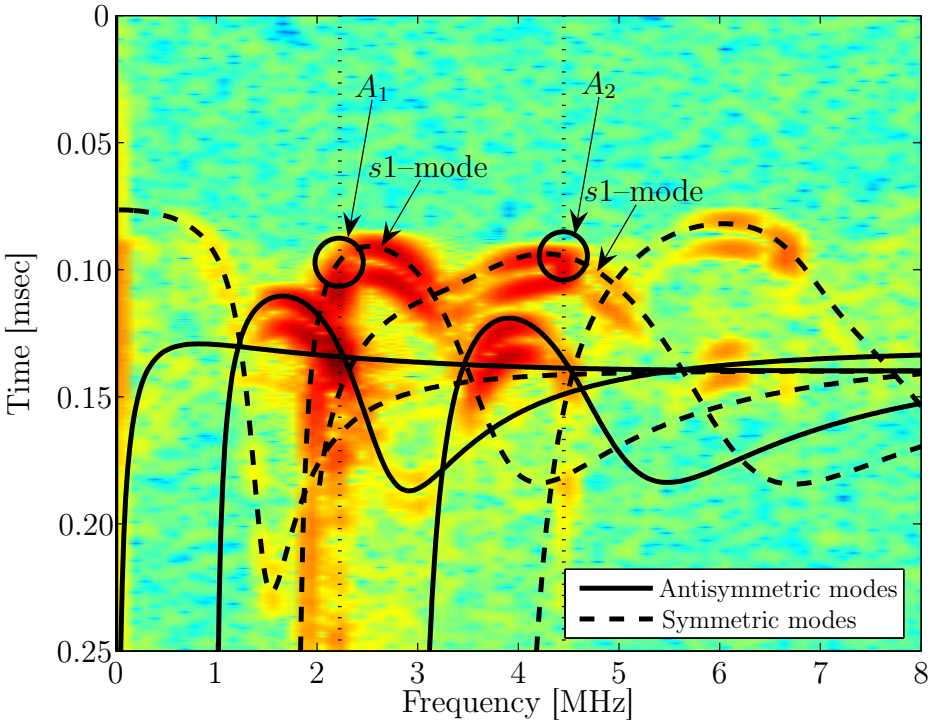

Figure 4.14: Spectrogram and dispersion curves.

It gives the energy density over the time for a first and second harmonic. The peaks becoming more distinct in this illustration and with the information of the spectrogram the different modes can identified clearly.

Compared to Bermes[3], who chosen a lower excitation frequency in his work, the $s1$–mode can clear separated from the $a1$–mode. The modes $s1$ and $s2$ arriving first, as expected. So they are not influenced by other modes. With the peaks (A_1) and (A_2) the relative nonlinearity ratio A_2/A_1^2 can be calculated for the evaluation of the experimental results in Chapter 5.

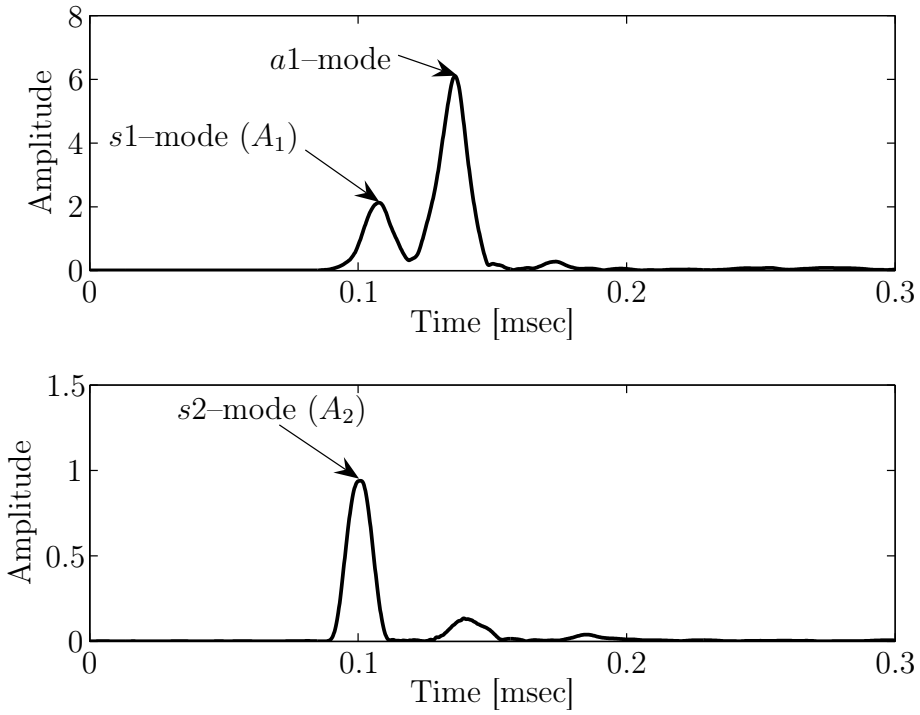

Figure 4.15: Fundamental and second harmonic frequency as functions of time.

CHAPTER V

EXPERIMENTAL RESULTS

With the nonlinear measurements as defined in Chapter 4, the increase of dislocation density due to plastic deformation has been detected and the results are described in this chapter. The specimens are statically loaded to different stain levels. For each specimen, the relative value A_2/A_1^2 is evaluated and assigned to different plastic strains. To get reliable results from the signal processing, the time window has to be adjusted to the given conditions. To demonstrate that the system setup and signal processing measure the cumulative effect of the second harmonic generation in the propagating lamb wave, first measurements for different propagation distances are done.

5.1 Evaluation of the system setup and signal processing

Bermes [4] verified that the measured material nonlinearity is not superposed from the introduced nonlinearity of the measurement setup. To identify the influence of the instrumentation nonlinearity, the input voltage for the transducer is increased. The value of A_2/A_1^2 did not change with increasing input voltage. This demonstrates that the experimental setup does not create a significant second harmonic frequency, which could distort the experimental results.

The objective is to generate Lamb waves with the correct conditions, that excite the cumulative second harmonic of a Lamb waves. To verify that the correct mode with the right frequency is excited to get a cumulative effect for the second harmonic, measurements for different propagation distances are preformed. On account of the

diffraction effect, the relative value A_2/A_1^2 should proportionally increase with the propagation distance [19]. To show that also a difference of the material nonlinearity can be detected, measurements for two aluminum plates with different alloys (Al 6061-T6 and Al 1100-H14) are executed. The propagation distance varied from 200 to 600 mm and the sheet thickness was 1.6 mm. For the signal processing with the short–time Fourier transformation a Hanning window of 256 points is used. The result with the best fitting straight lines is given in the Figures 5.1. The ratio A_2/A_1^2 for the two aluminum plates is plotted over the propagation distance. The linear increase of

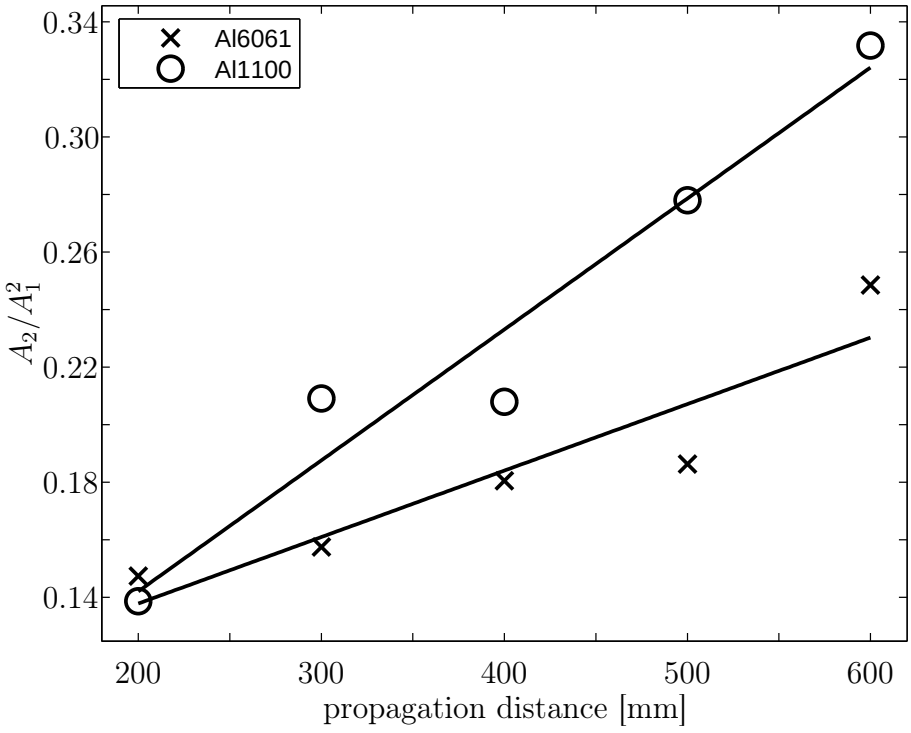

Figure 5.1: Relative nonlinearity value A_2/A_1^2 over the propagation distance for the two different aluminum alloys.

A_2/A_1^2 with the propagation distance is the evidence that the excited second harmonic is cumulative for the chosen setpoint. Also the relative values of A_2/A_1^2 are higher for the Al 1100-H14 plate than for the Al 6061-T6 plate, which agrees with the experimentally determined absolute nonlinearity values β [32]. The absolute value,

measured with longitudinal waves is for Al 1100-H14 $\beta = 12.0$ and for Al 6061-T6 $\beta = 5.67$. To compare this with relative Lamb wave measurements the ratio of the different material nonlinearities is calculated.The absolute ratio from the longitudinal measurements $\beta_{Al1100}/\beta_{Al6061}$ is 2.12. With the fundamental frequency choice of $f = 2.225\,\mathrm{MHz}$ and a separation of the $s1$–mode from the influencing $a1$–mode the ratio of the relative nonlinearities of the Lamb wave measurements came closer to the absolute ratio from the nonlinear longitudinal measurements. The derived ratio from the Lamb wave measurements is 1.89 compared to the ratio of 2.58 from previous Lamb wave measurements [4]. This demonstrates that it is feasibility to detect the material nonlinearity with the applied system setup and signal processing.

5.2 The impact of the short–time Fourier transformation window length

Even with the wedge excitation method, is it not possible to generate only the s1–mode. Also the a1–mode is excited. But with the short–time Fourier transformation as described in Chapter 4, is it feasible to identify the single modes in the time–domain wave signal and to specify the amplitudes A_1 for the $s1$–mode and A_2 for the $s2$–mode. After a certain propagation distance, the individual modes are well separated. However, if the propagation distance is not so far, the modes overlap and influence each other. Figures 5.2 and 5.3 shows the amplitudes of the fundamental and second harmonic Lamb wave for 200 mm and 400 mm. The big amplitude of the $a1$–mode can impact in the $s1$–mode. This leads to the result that erroneous values for the mode amplitude A_1 and A_2 are displayed by the signal processing.

By examining the spectrograms from measurements before and after plastic deformation a change of wave modes curves is visible. The wave modes propagating apparently not as close "packages" due to the changes of the material properties (Figures 5.4 and 5.5). The spreading out of the modes is particularly easy to observe

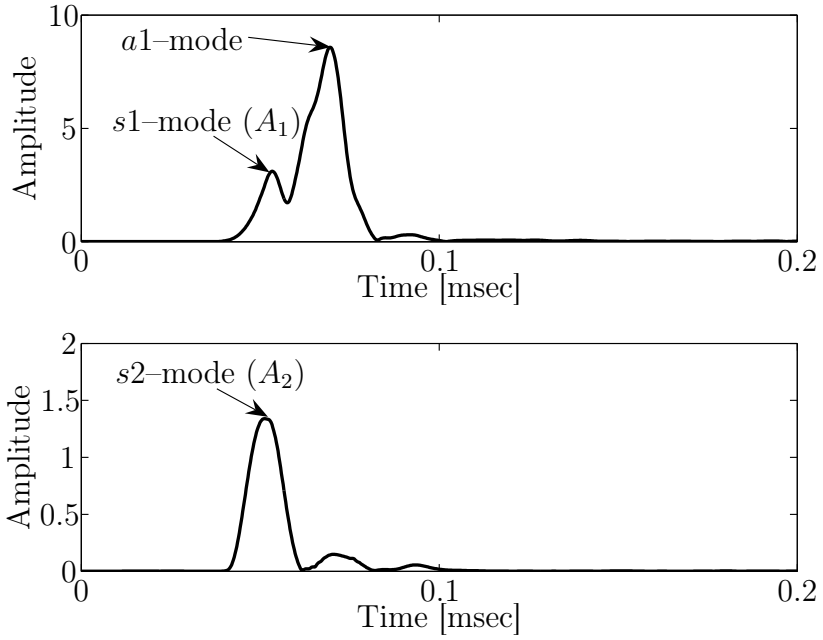

Figure 5.2: Fundamental and second harmonic frequency as functions of time after wave propagationed a distance of 200 mm.

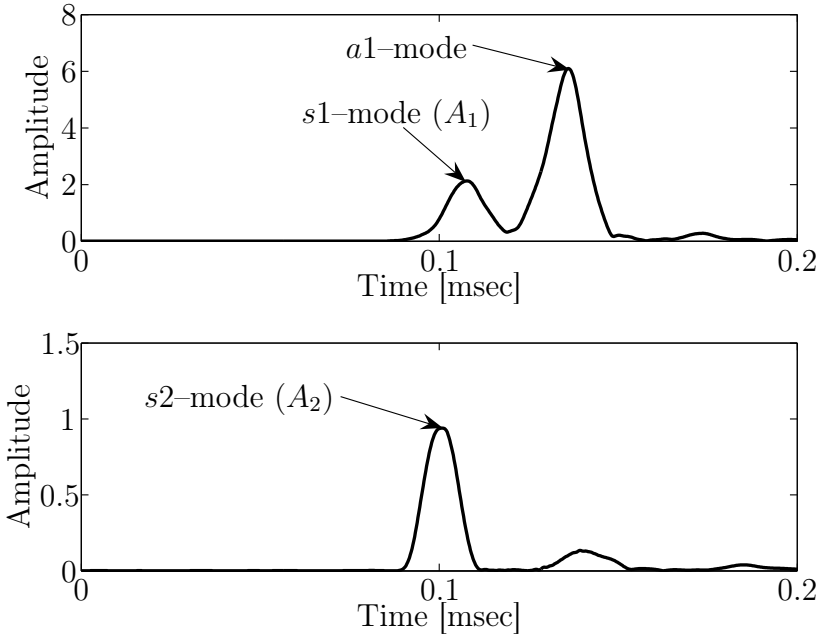

Figure 5.3: Fundamental and second harmonic frequency as functions of time after wave propagationed a distance of 400 mm.

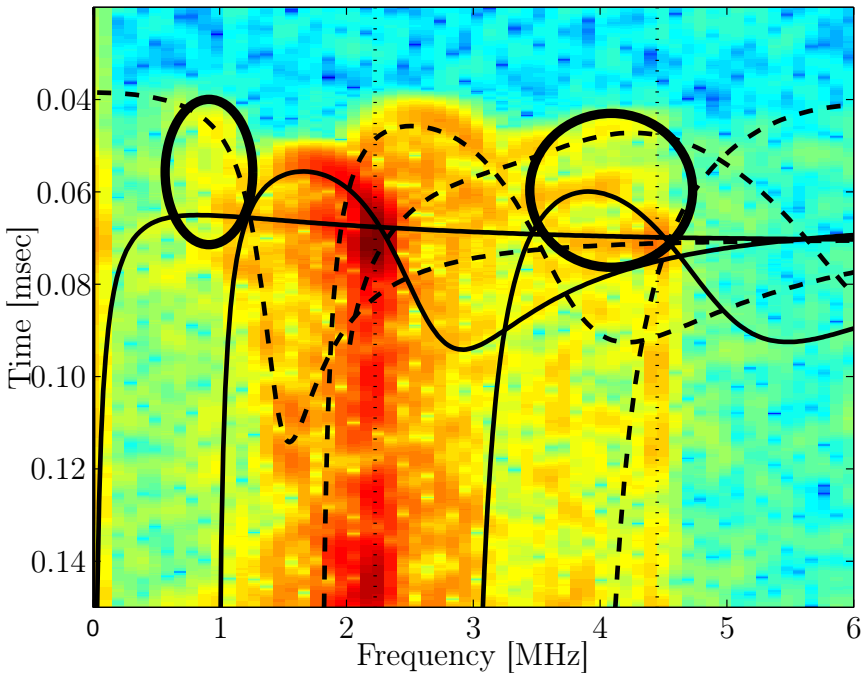

Figure 5.4: Spectrogram from measurement on a specimen with no plastic deformation.

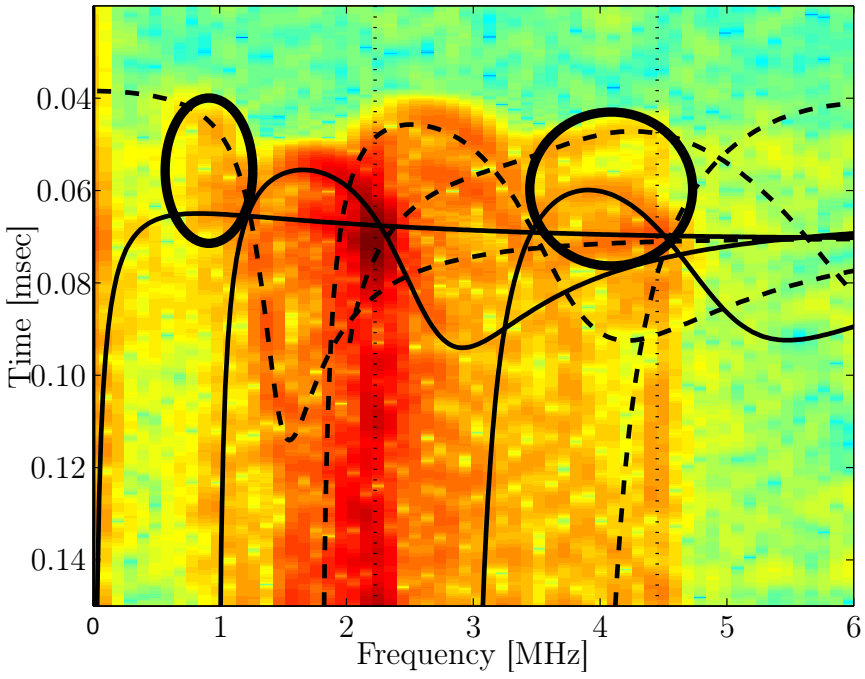

Figure 5.5: Spectrogram from measurement on a specimen with plastic deformation.

in the marked areas. For short propagation distances this effect makes it harder to separate the individual modes with the signal processing.

Because of the described effects, the choice of the short–time Fourier transformation window size has to be done in a clever fashion. To assure that the modes are separated completely from the signal processing, the window length has to be adjusted to the given experimently conditions. With a more narrow window the time resolution improves and the modes are not overlapping and influencing each other (Figures 5.6 and 5.7). Niethammer [27] showed that due to Heisenberg uncertainty principle, a simultaneous increase of the resolution for time and frequency is not possible (see Appendix A for details). A more narrow window size increases the time resolution, but at the same time worsens the frequency resolution. This is not a disadvantage for the Lamb wave measurements with the chosen s1 $\rightarrow$ s2 setpoint. At the time when the s1–and s2–modes arrive, no other mode is in the frequency region of fundamental and second harmonic arriving.

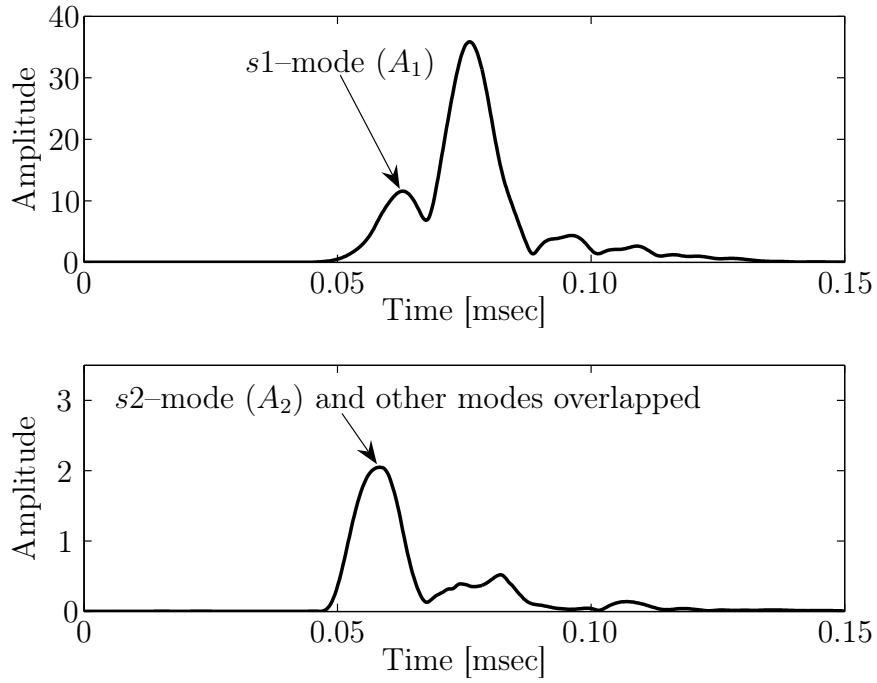

Figure 5.6: Fundamental and second harmonic frequency as functions of time evaluated with wide Fourier Transformation window.

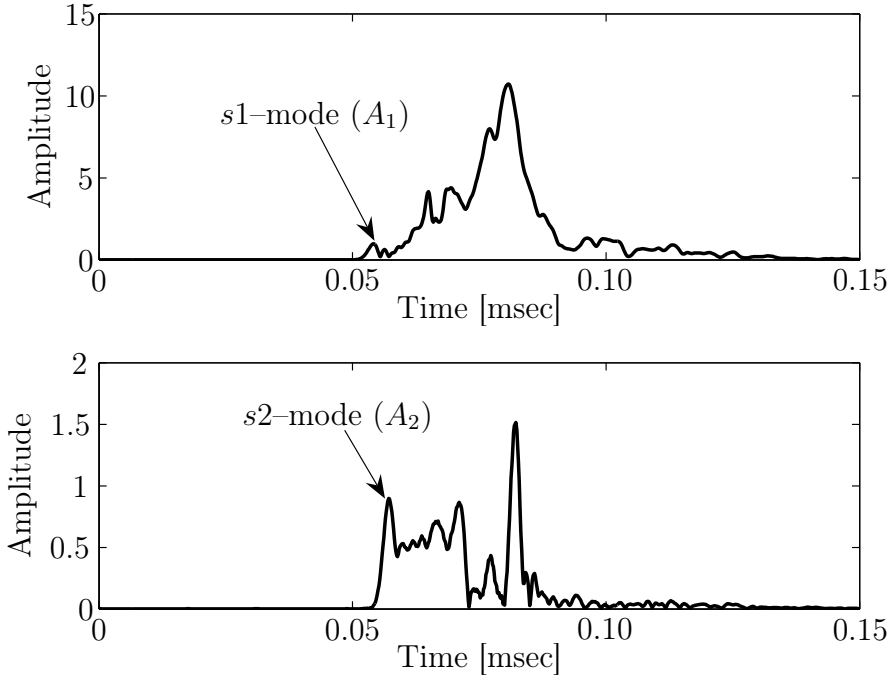

Figure 5.7: Fundamental and second harmonic frequency as functions of time evaluated with narrow Fourier Transformation window.

5.3 Assessment of material nonlinearity change due to plastic deformation

Plastic deformation increases the dislocation density in a material. This damage of the microstructure causes material nonlinearity, so more second order harmonic waves are excited when the wave propagates through the material. To demonstrate that this can be detected with ultrasonic Lamb wave measurements, specimens are loaded over yield so that plastic deformation occurs. Six specimens with the dimensions illustrated in Chapter 4 are prepared from the same batch of material. Each specimen is loaded statically to different final loads above yield. The stress–strain curve for the aluminum and the load points for the different specimens is given in Figure 5.8. The corresponding values can be found in Table 5.1.

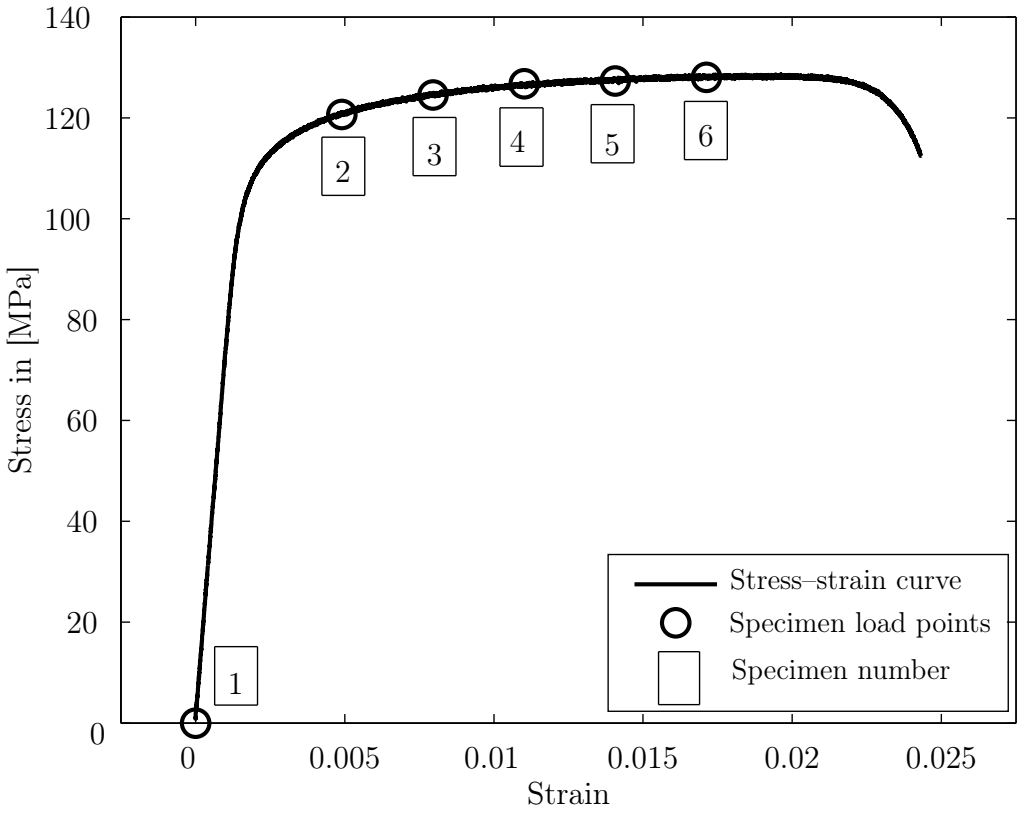

Figure 5.8: Stress–strain curve with load–points for the different specimens.

Table 5.1: Data tables for the different stress and strain level of the specimens.

specimen–number	1	2	3	4	5	6
max. stress [MPa]	0	120.66	124.53	126.75	127.31	128.02
strain at max. load	0	0.0049	0.0080	0.0110	0.0141	0.0171
plastic strain	0	0.0019	0.0062	0.0093	0.0123	0.0154

The specimen with the most load (specimen 6) was loaded close to ultimate strength of the material. Over the ultimate strength necking occurs. That would influence the measurements. Lamb wave measurements are performed on the unloaded specimens. Both detection methods are applied. The propagation distance for the laser interferometer was 200 mm and for the wedge detection was 220 mm. The measurements are repeated three times. Thereby, the wedge(s) were completely removed and re–coupled for every measurement to avoid the influence of improper coupling. The average of the three measurements is calculated for the amplitudes of A_1 and A_2 and the ratio A_2/A_1^2. The evaluated relative values A_2/A_1^2 are normalized by the relative value measured before the specimens were loaded. This extracts the innate material nonlinearity. The determined values are plotted over the plastic strain of the specimens. For normalized ratios A_2/A_1^2 also the error bar from the three measurements is illustrated. Note that the thickness of the specimens only changed a maximum of 1.3 % due to the platic deformation. This results in a insegnificant change of the excitation condition of the cumulative second harmonic generation and has therefore no effect on the measurements. To demonstrate the importance to adapte the short–time Fourier transformation window in the signal processing the

measured wave signals are analysed with two different window sizes.

5.4 Analysis of the detected signal with a wide short–time Fourier transformation window

For the analysis of the the measurement results with the use of the laser interferometer for wave detection a Hanning window with size of 201 points for the short–time Fourier transformation are chosen. For the wedge detection a the window size of 256 points was applied. In the Figures 5.9, 5.10, 5.11 and 5.12 the amplitudes for the s1–mode A_1 and the s2–mode A_1 is plotted for the each specimen. Both for the wave detection with laser interferometer and wedge method an increase of A_1 and A_2 can be observed. The increase of A_2 was expected due to the accumulation of the dislocation density. The material nonlinearity raised and cumulative second harmonics has been excited more. But the amplitude A_1 should be constant since the first harmonic is independent of the material nonlinearity. The increase is induced by the $a1$–mode. The $s1$–mode and the $a1$–mode overlapping each other when a wide window for the short–time Fourier transformation is applied. With more plastic deformation the influence of the $a1$–mode is stronger, because the mode‘s spreading more.

In the Figures 5.13 and 5.14, the normalized nonlinearity values A_2/A_1^2 are assigned over strain for the laser interferometer and wedge method wave detection. The bar diagrams show the mean value of three measurements. In the second plot, the error bars of measurements are shown. For the measurements with the laser interferometer A_2/A_1^2 keeps almost constant and for the measurements with the wedge method a decrease of A_2/A_1^2 is to see. This does not agree with what has theoretically and experimentally been derived in previous works [7, 8, 20, 25]. An increase of A_2/A_1^2 should arise from the measurements. The reason for this is that the amplitude A_1 for the s1–mode is much bigger than the amplitude A_2 for the s2–mode and in addition the amplitude A_1 is in squared in the nonlinearity value A_2/A_1^2. So the

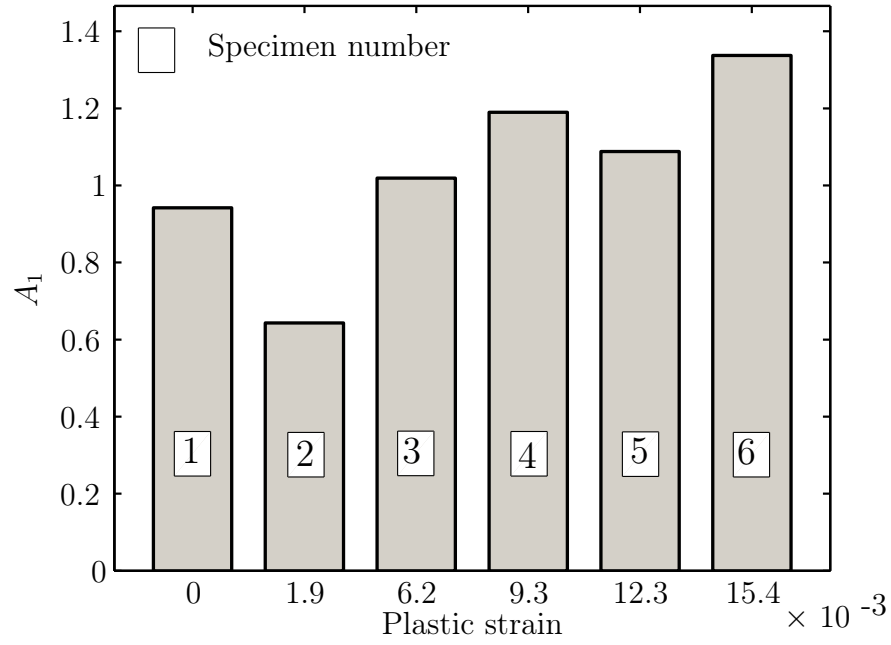

Figure 5.9: A_1 over the plastic strain detected with the laser interferometer and a wide short–time Fourier transformation window.

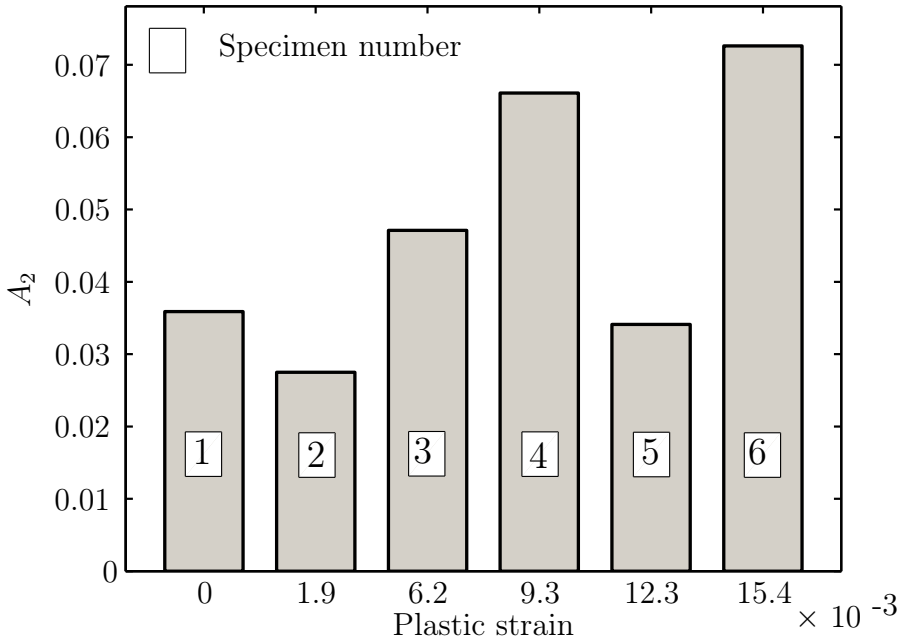

Figure 5.10: A_2 over the plastic strain detected with the laser interferometer and a wide short–time Fourier transformation window.

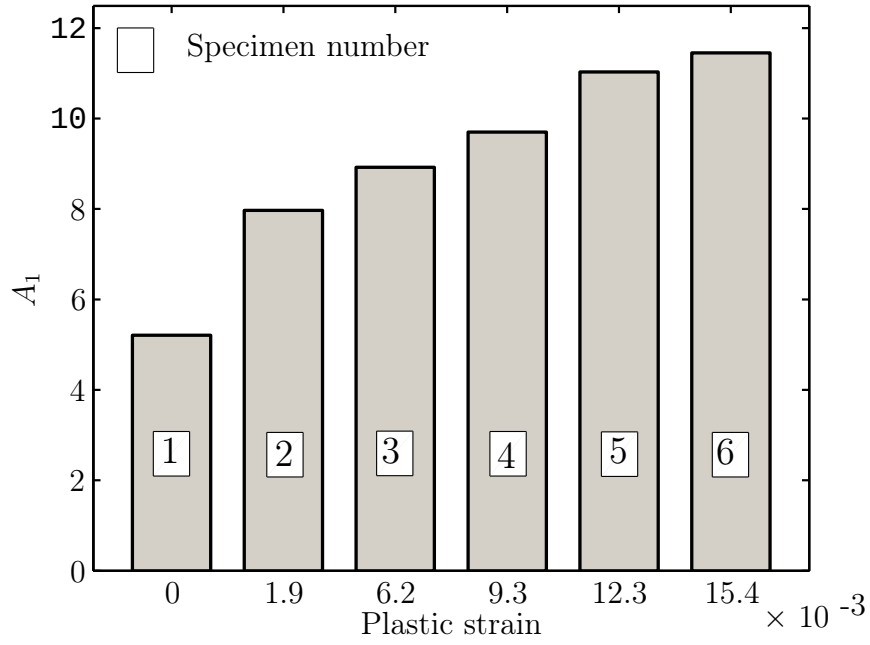

Figure 5.11: A_1 over the plastic strain detected with the wedge method and a wide short–time Fourier transformation window.

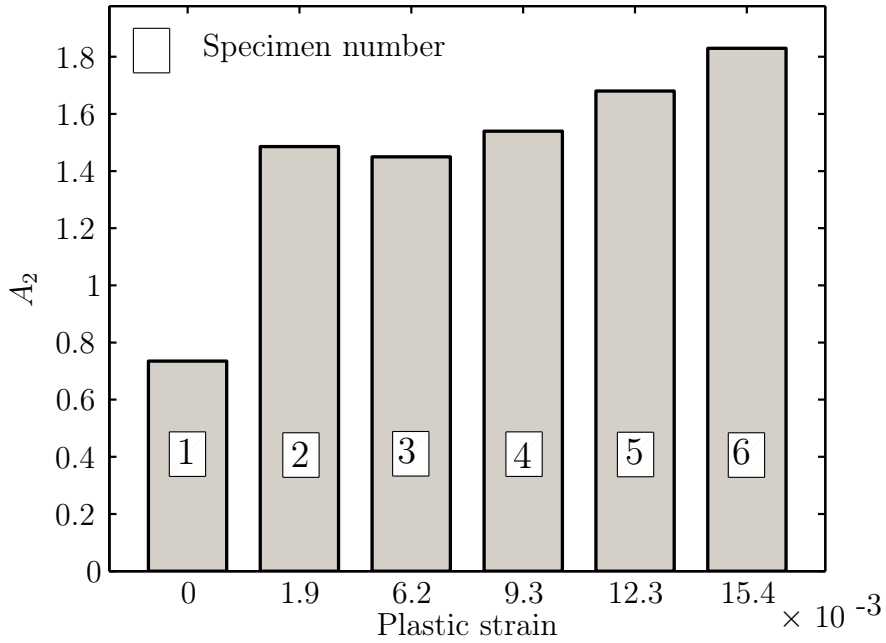

Figure 5.12: A_2 over the plastic strain detected with the wedge method and a wide short–time Fourier transformation window.

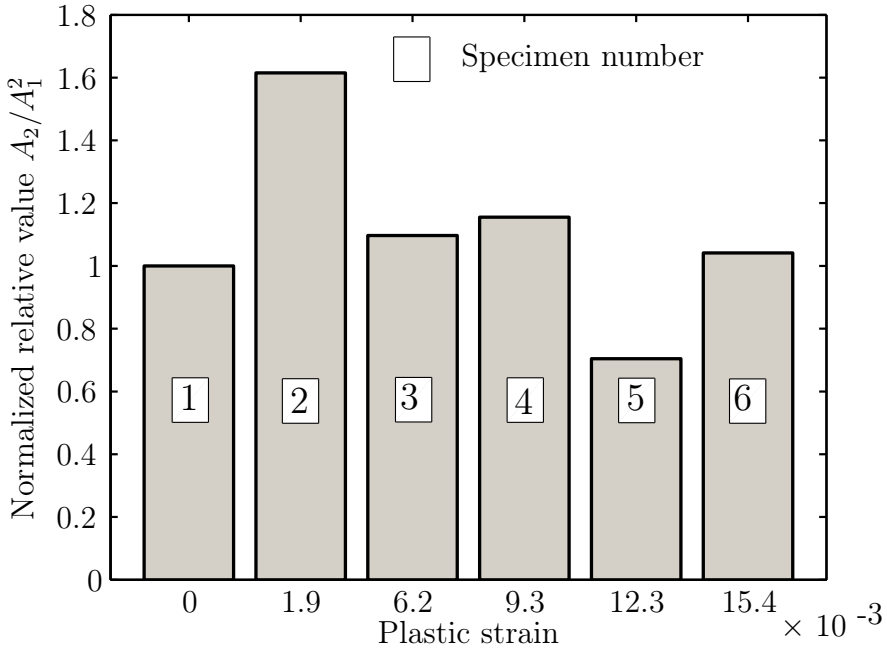

(a) Mean values of the measurements

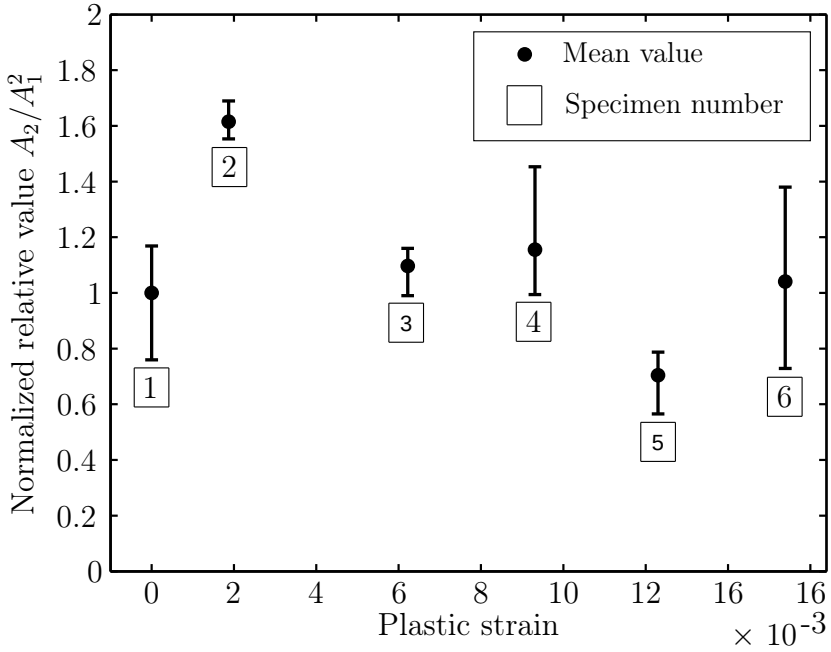

(b) Mean values and error bars of the measurements

Figure 5.13: Normalized relative value A_2/A_1^2 over the plastic strain detected with the laser interferometer and a wide short–time Fourier transformation window.

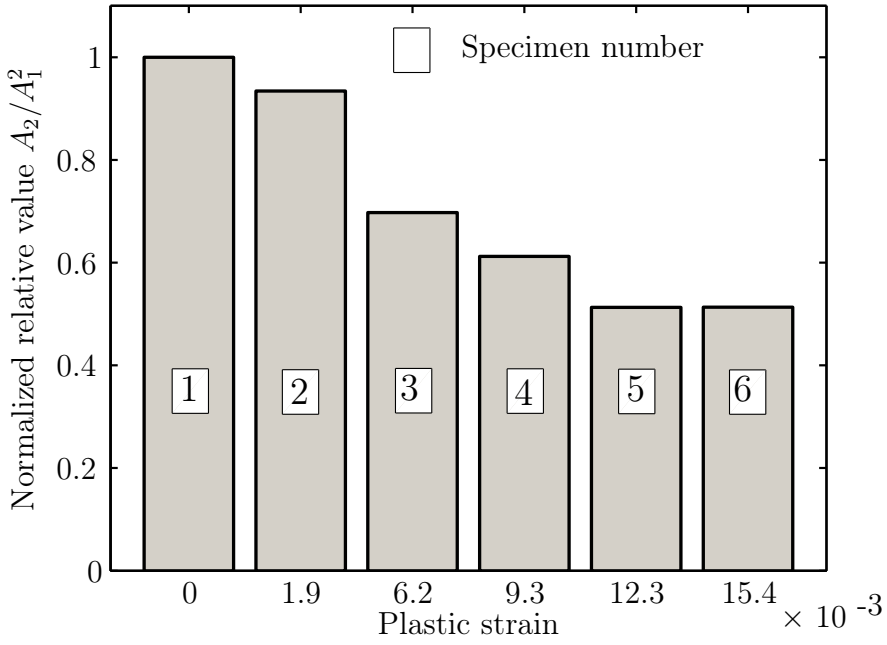

(a) Mean values of the measurements

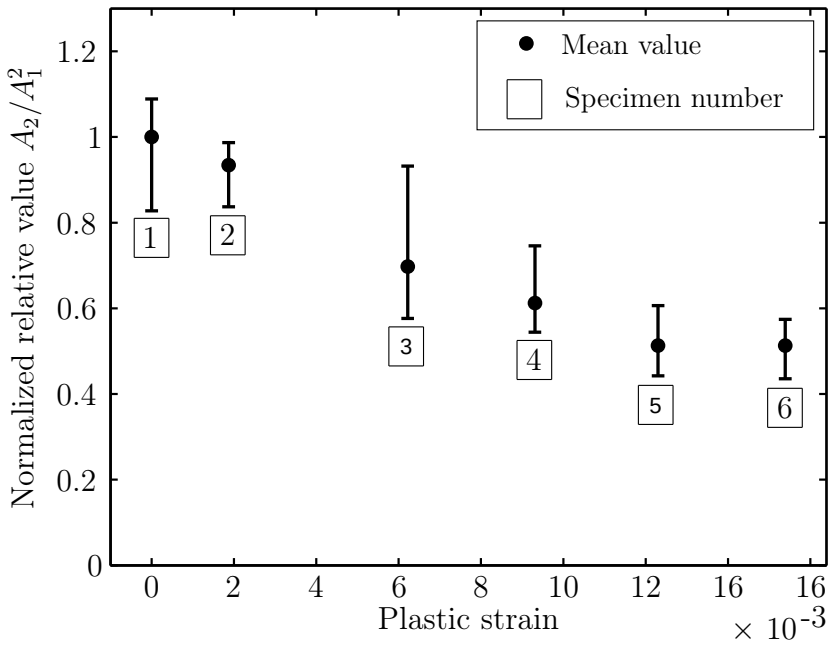

(b) Mean values and error bars of the measurements

Figure 5.14: Normalized relative value A_2/A_1^2 over the plastic strain detected with the wedge method and a wide short–time Fourier transformation window.

increase of the amplitude A_1 due to the signal processing with the wide short–time Fourier transformation window leads to incorrect relative ratios A_2/A_1^2. An increase in the material nonlinearity due to the plastic deformation could not be ascertained.

5.5 Analysis of the detected signal with a narrow short–time Fourier transformation window

To avoid that the modes overlapping the size of short–time Fourier transformation window is reduced. A Hanning window with 64 points is taken for analysis of the measured wave signals. This window size is used for both measurements, the measurements with the laser interferometer and with the wedge method. Again, the amplitudes for the s1–mode, A_1 and the $s2$–mode, A_1 are plotted for each specimen (Figures 5.15, 5.16, 5.17 and 5.18). With the new signal analysis the amplitude, A_1 should now be constant. The $a1$–mode no longer affects the $s1$–mode, even the modes spreading more with higher plastic deformation. But a decrease of A_1 can be observed for the measurements with the laser interferometer. This is caused by the effect that the modes are spreading out, and so the amplitudes decrease relatively with higher plastic deformation. With the averaging effect over an area with the wedge detection method, the impact of the mode spreading is not so strong and the amplitude A_1 is constant for the different measurements. Also, the detected amplitude A_2 of the $s2$–mode is influenced by the mode spreading effect. Consequently A_2 decreases with more plastic strain even though it should increase.

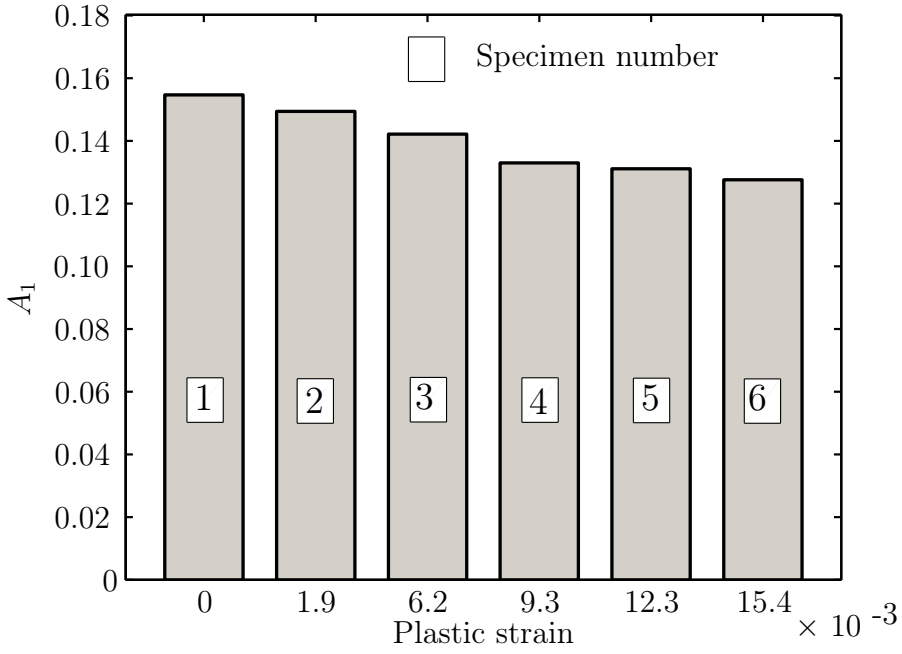

Figure 5.15: A_1 over the plastic strain detected with the laser interferometer and a narrow short–time Fourier transformation window.

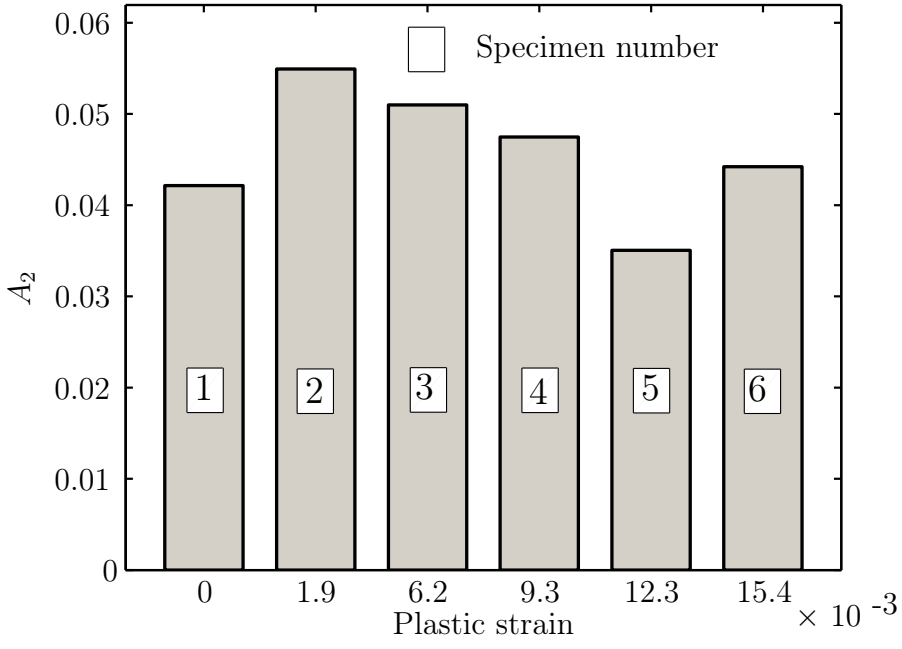

Figure 5.16: A_2 over the plastic strain detected with the laser interferometer and a narrow short–time Fourier transformation window.

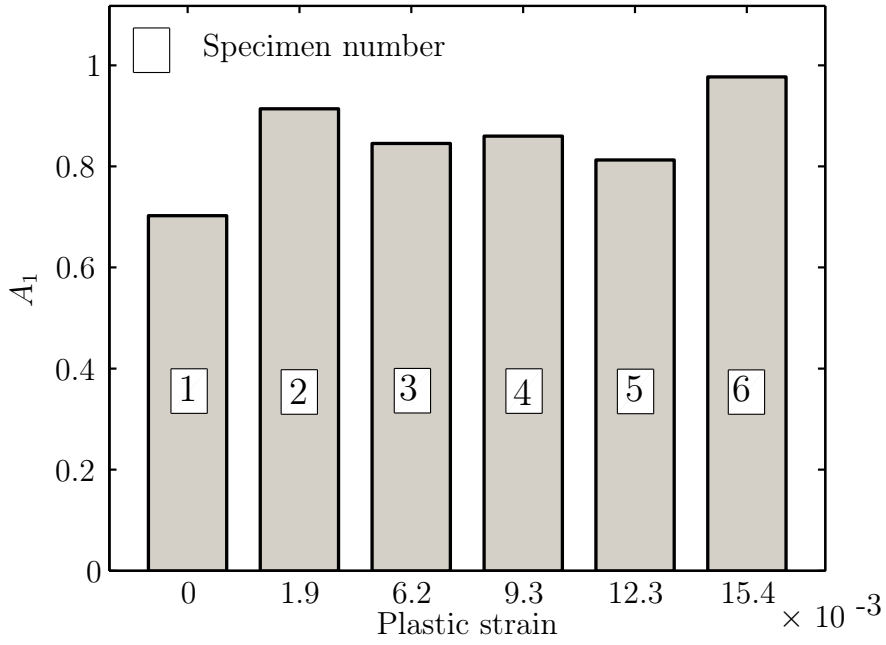

Figure 5.17: A_1 over the plastic strain detected with the wedge method and a narrow short–time Fourier transformation window.

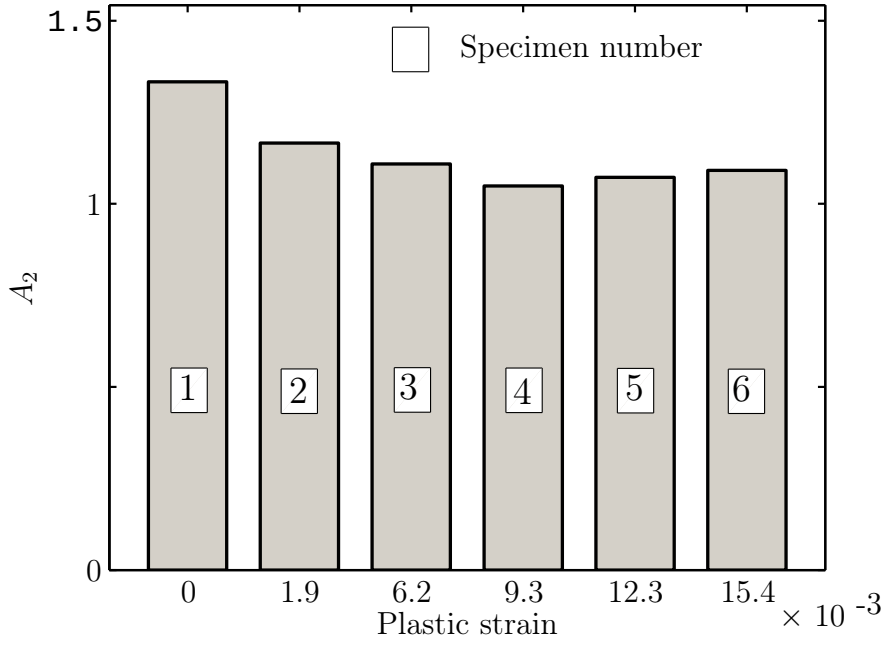

Figure 5.18: A_2 over the plastic strain detected with the wedge method and a narrow short–time Fourier transformation window.

The Figures 5.19 and 5.20 show the relative values A_2/A_1^2 determined with the narrow short–time Fourier transformation window. The normalized relative values are plotted for the different specimens determined with the laser interferometer and wedge method wave detection. A increase of the ratio A_2/A_1^2 is visible for the both wave detection techniques. This increasing trend conforms with the results obtained with longitudinal and Reyleigh wave measurements [21, 25].

It can be demonstrated that for short propagation distances and with the influence of the mode spreading effects, an adjustment the short–time Fourier transformation window is necessary. The reduction of the window size increases the time resolution and the modes do not influence each other any more. Therefore, with the narrow window size an increase of the material nonlinearity due to plastic deformation is detected with the proposed Lamb wave measurements. Measuring of the propagating Lamb wave with a wedge has the advantage that the spreading effect has not so much influence on the amplitudes A_1 and A_2. But also with the application of the laser interferometer to detect the wave the change of the material nonlinearity can be determined. The stronger increase of the relative value A_2/A_1^2 with growing plastic deformation detected by the wedge–transducer combination is caused by the amplification of the second harmonic due to the inherent resonance of the transducer. The second harmonic frequency is closer to the center frequency of the detection transducer than the first harmonic frequency. The lower value of material nonlinearity of the specimen number 5 could be observed with both detection methods.

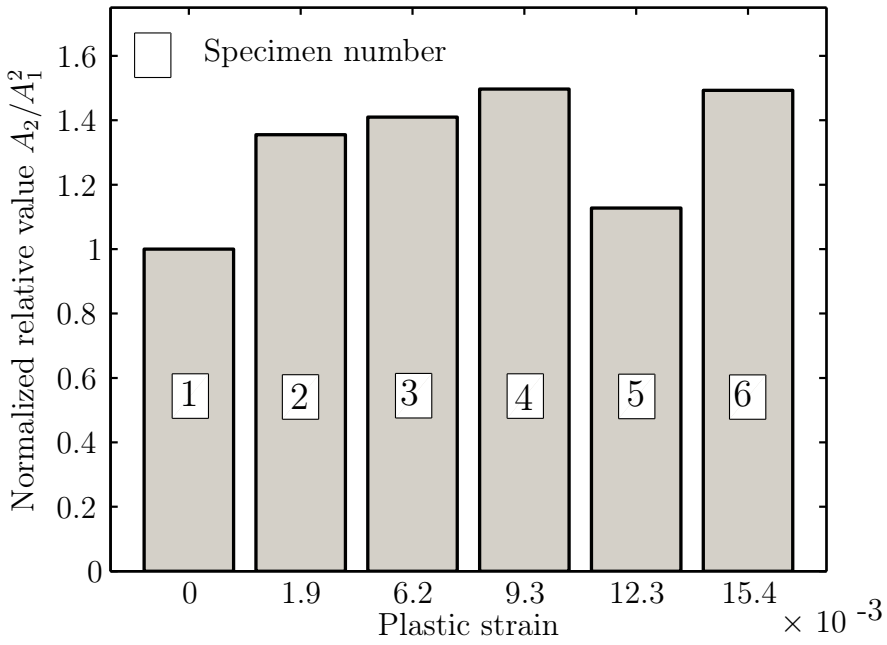

(a) Mean values of the measurements

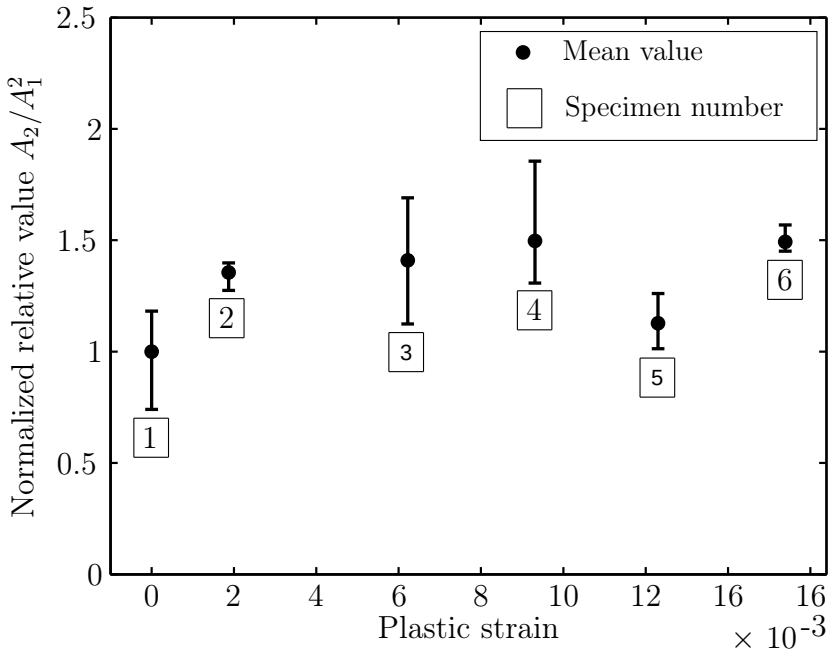

(b) Mean values and error bars of the measurements

Figure 5.19: Normalized relative value A_2/A_1^2 over the plastic strain detected with the laser interferometer and a narrow short–time Fourier transformation window.

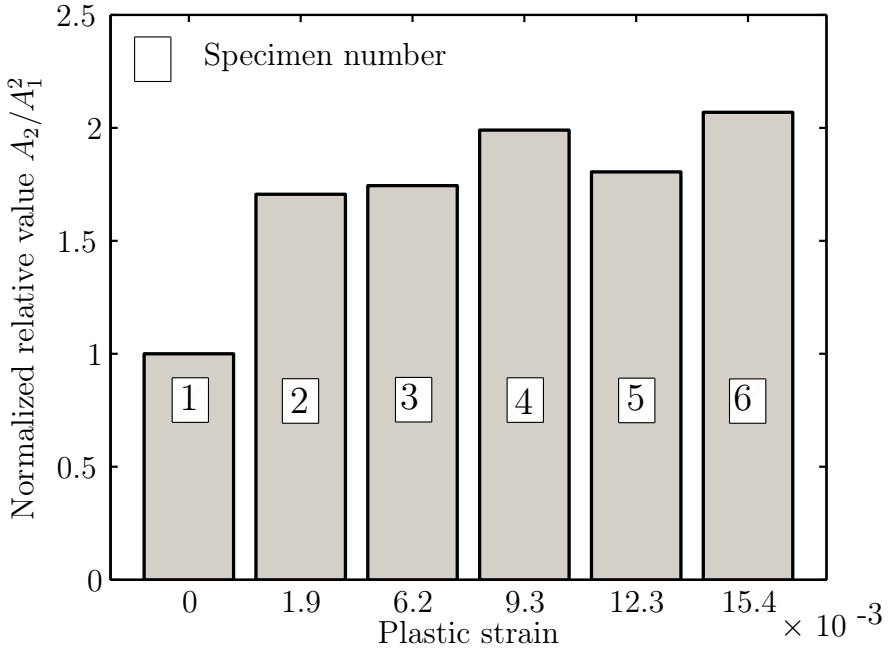

(a) Mean values of the measurements

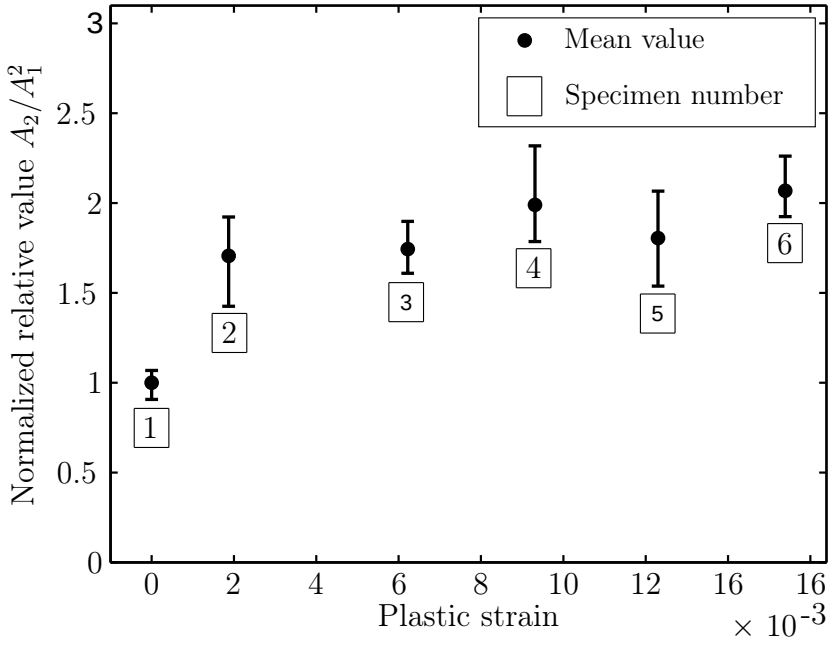

(b) Mean values and error bars of the measurements

Figure 5.20: Normalized relative value A_2/A_1^2 over the plastic strain detected with the wedge method and a narrow short–time Fourier transformation window.

CHAPTER VI

CONCLUSIONS AND FURTHER WORK

In this thesis Lamb wave measurements are performed to detect an increase of material nonlinearity due to plastic deformation. Under certain conditions, the propagating Lamb wave generates cumulative second harmonic waves, which can be used to track material nonlinearity.

In the experimental setup, the wedge generation method was employed to launch the fundamental wave. The design of the wedge is improved to generate a significantly higher wave displacement amplitude. The propagation distance of the wave in the wedge is reduced and a clamping fixture for the transducer has been designed so that oil could be used as couplant between transducer and wedge. The phase θ could be made bigger, so that the edge of the wedge is closer to the acoustical axis. This reduced the excitation energy component which goes in to the unintentional excited $a1$–mode. Also, the coupling of the wedge to the specimen is an important factor in the measurements. A great part of the measurement inaccuracy comes from bad coupling of the wedge to the specimen [23]. To increase the reliability of the measurements, the fixing of the wedge should be advanced to make the measurements more robust.

For the detection of the propagating wave a laser interferometer and wedge–transducer combination are used and their advantages and disadvantages are discussed. To separate the modes in the detected wave signal, a short–time Fourier transformation (STFT) is applied.

To verify that the experimental setup is sufficient to measure material nonlinearity with Lamb waves, measurements are executed for various distances on two aluminum

sheets with different alloys. A linear increase of the relative value A_2/A_1^2 with increasing propagation distance was observed. This agrees with theoretical and experimental works and shows that the measured second harmonic frequency is not created by the experimental setup, but in fact due to inherent material nonlinearity. The relative ratio of the material nonlinearity from the two alloys has been measured and compared with the ratio measured with longitudinal waves. With a better fundamental frequency choice, and the separation of the $s1$–mode from the $a1$–mode, the ratio measured with Lamb waves came closer to the value of the absolute nonlinear longitudinal measurements.

To assess the change of material nonlinearity due to plastic deformation, six specimens are loaded over yield so that plastic deformation occurs. The specimens length was limited by the load frame dimensions. The relatively short specimens and the mode spreading with increasing plastic deformation made the mode separation with the short–time Fourier transformation more difficult. To illustrate the influence of the short–time Fourier transformation window length on the possibility to separate the modes, the detected signals from the Lamb wave measurements are analyzed with a wide and narrow window. With the narrow window, the modes can be better separated since the time resolution is better. The measured relative nonlinearity value A_2/A_1^2 increases with plastic deformation as expected. That the frequency resolution worsens with the reduction of short–time Fourier transformation window length had no influence on the experimental results. No other modes are in the frequency region of the fundamental and second harmonic, when the $s1$–and $s2$–mode arrive. The measurement results showed that with both wave detection methods (laser interferometer and wedge–transducer combination) the propagating Lamb wave can be detected well and the material nonlinearity can be reliable characterized. The Lamb wave measurements seem to be a robust technique to characterize the relative nonlinearity of a material.

With the wedge method for the wave detection, the modes amplitudes of $s1$ and $s2$ increased. When the center frequency of the detection transducer is chosen close to the second harmonic frequency, the relatively weak second harmonic displacement field is recorded additionally stronger. To further extract the low second harmonic wave signal, components from the strong first harmonic signal can be split into two signals. One part can be used to acquire the first harmonic components. The second part is sent in an appropriate narrow bandpass filter and low–noise amplifier. This gives a high second harmonic signal with no influence of the first harmonic.

When in future the absolute nonlinearity parameter β will be determined, the absolute measure of the wave displacement is necessary. Measurements with laser interferometry are then the more useful way, since the displacement is direct related to the wavelength. Further, the laser interferometer is truly broadband. All frequency components are detected equally and are not tempered by the frequency resonance of the detection transducer.

To verify that the Lamb wave measurement are suitable for the assessment of material fatigue life, cycling loading test should be performed as done in other works [16, 21]. A strong increase should observable since cycling loading increase highly the dislocation density in a material.

APPENDIX A

LIMITATION OF THE SHORT–TIME FOURIER TRANSFORMATION RESOLUTION DUE TO THE HEISENBERG UNCERTAINTY

A short–time Fourier transformation (STFT) is a suitable technique to determine quantitative changes of the frequency content of signal as function of the time. However, there are limitations in resolution. The short–time Fourier transformation and the representation in a spectrogram are restricted by the Heisenberg uncertainty. The term uncertainty is misleading. The effect is complete predictable. Due to Heisenberg uncertainty is in not possible to get with the short–time Fourier transformation a ideal resolution in time and frequency at the same time.

For the derivation of the uncertainty principle some prefatory definitions are necessary.

The square norm $\|s(t)\|$ of a function $s(t)$ is given by

$$\|s(t)\| = \left(\int_{-\infty}^{\infty} |s(t)|^2 \mathrm{d}t \right)^{\frac{1}{2}} . \tag{A.1}$$

The definition of the normalized function $s_n(t)$ is

$$s_n(t) = \frac{s(t)}{\|s(t)\|}. \tag{A.2}$$

Because the square norm of a normalized function is one, the squared magnitude can be seen as a probability density. With the squared magnitude is it feasible to compute

the mean time of function $s(t)$ with

$$E[t] = \int_{-\infty}^{\infty} t|s_n(t)|^2 \mathrm{d}t \tag{A.3}$$

and the mean angular frequency with

$$E[\omega] = \int_{-\infty}^{\infty} \omega|S_n(\omega)|^2 \mathrm{d}\omega. \tag{A.4}$$

$S_n(\omega)$ stays the normalized Fourier transform of the time function $s(t)$. The variances for t and ω can be obtained with

$$\sigma_t^2 = \int_{-\infty}^{\infty} (t - E[t])^2|s_n(t)|^2 \mathrm{d}t \tag{A.5}$$

and

$$\sigma_\omega^2 = \int_{-\infty}^{\infty} (\omega - E[\omega])^2|S_n(\omega)|^2 \mathrm{d}\omega. \tag{A.6}$$

The resolution is restricted by the uncertainty principle to

$$\sigma_t^2 \sigma_\omega^2 \geq \frac{1}{4}. \tag{A.7}$$

For this reason the standard deviation of the time and frequency can not changed independent from each other.

The value of time–frequency spread depends on the used time window. With the equations above the time–frequency spread for different window types can be calculated. The minimum value of $\frac{1}{4}$ in Equation (A.7) is only possible for the functions of the form

$$s(t) = ae^{i\xi t}e^{-b(t-u)^2}. \tag{A.8}$$

or a product of a complex harmonic multiplied with a Gaussian. For a Hanning window, which is used in this work, the time–frequency spread $\sigma_t^2\sigma_\omega^2$ is 0.5133.

The time resolution is optimal in the time domain and the frequency resolution is optimal in the Fourier domain representation as illustrated in Figure A.1. But in this representation a resolution of the frequency or respectively of the time is not available. If a representation of the signal simultaneously in time–and frequency–domain is necessary, like for the Lamb wave signal processing in this work, the resolution is limited by the uncertainty principle. Not both resolution can be optimized at the same time. In a short–time Fourier transformation the resolution depends only on the time–window size. A wide window gives a better frequency resolution, but worse the time resolution. On the other hand a more narrow window gives a better frequency resolution, but worse the time resolution. This is shown in Figure A.2.

To illustrate the influence of the window size on the resolution the frequency and time variations are calculated [27]. In Figure A.3a a normalized Hanning window is illustrated and Figure A.3b shows the Fourier transform of the window. For the calculations a sampling frequency for the time signal of 100 MHz is chosen. So 1000 points representing 10 μs of the signal. Figure A.3c shows time deviation over the window length. A increase in the window length results in a larger time deviation. Additionally the time variance σ_t is illustrated. In Figure A.3d and A.3e, σ_t and σ_f are assigned over the window length in points. It can be seen, that a too narrow window results in a large frequency standard deviation. But on the other hand, a too wide window gives a large time standard deviation. So a compromise has to be found, which fits best to the resolution requirements.

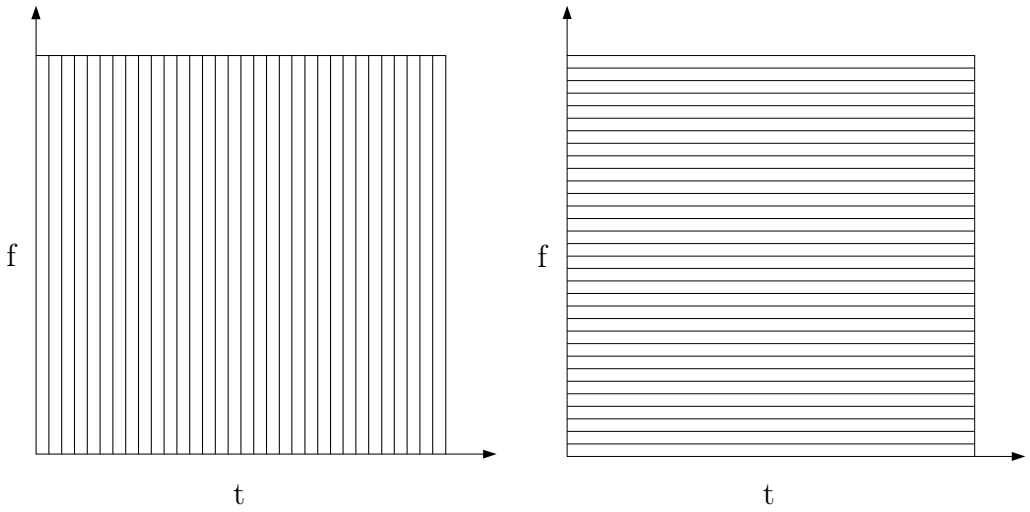

(a) Time domain representation (b) Fourier domain representation

Figure A.1: Time and Fourier domain signal representations

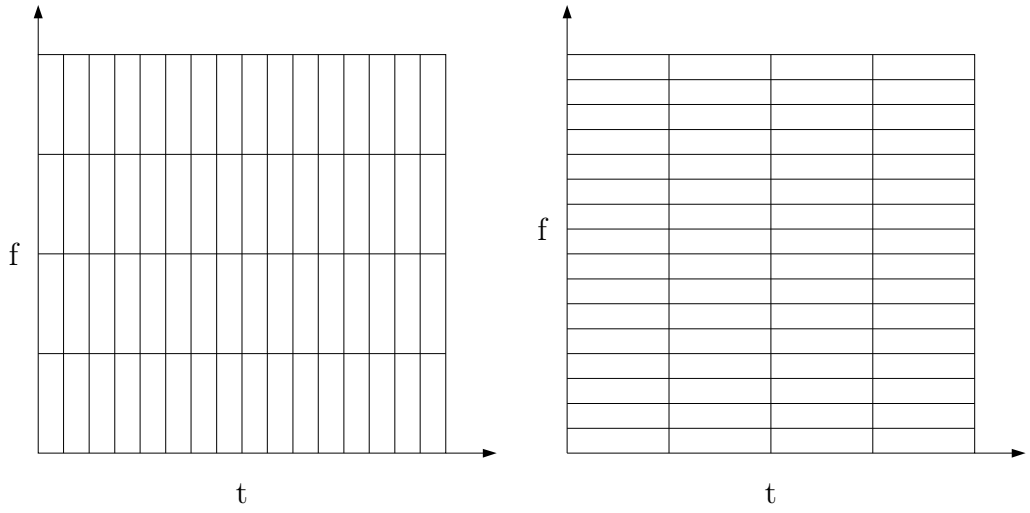

(a) STFT domain representation with a narrow window (b) STFT domain representation with a wide window

Figure A.2: STFT signal representations

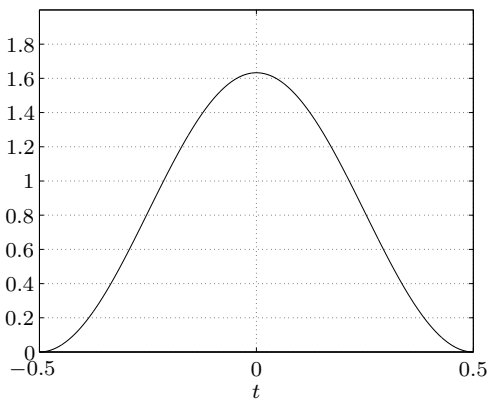

(a) Normalized Hanning window

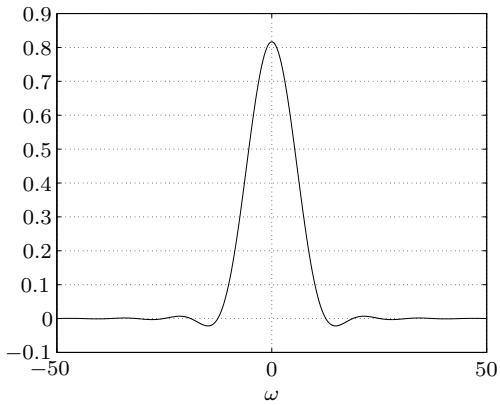

(b) Fourier transform of a Hanning window

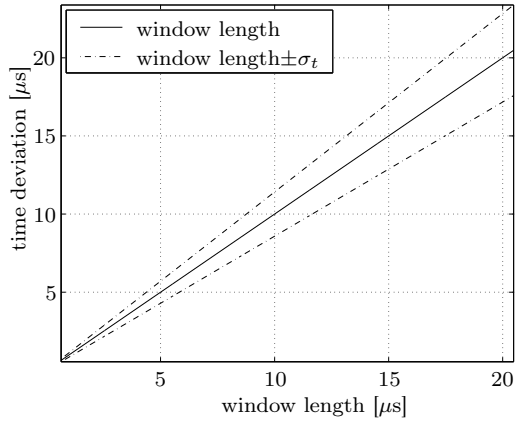

(c) Time uncertainty

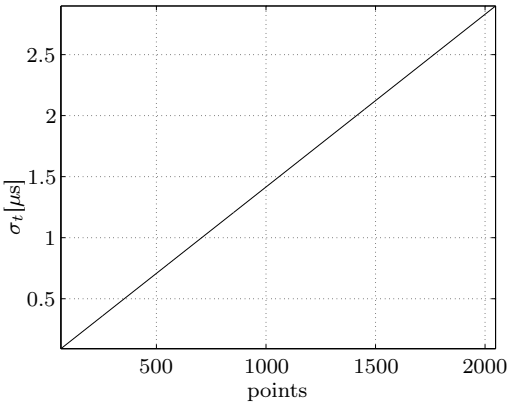

(d) Time uncertainty

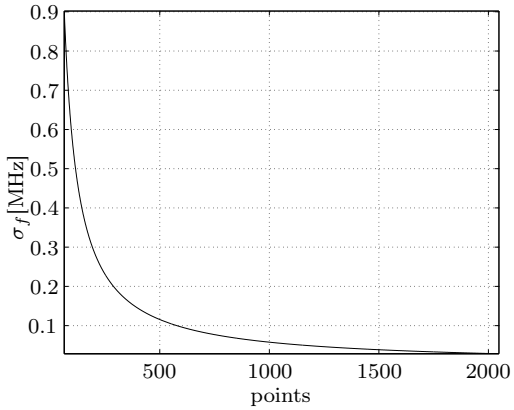

(e) Frequency uncertainty

Figure A.3: STFT with Hanning window

REFERENCES

[1] Achenbach, J. D., *Wave Propagation in Elastic Solids*. North–Holland, first ed., 1975.

[2] Barnard, D. J., Dace, G. E., and Buck, O., "Acoustic harmonic generation due to thermal embrittlement of inconel 718," *Journal of Nondestructive Evaluation*, vol. 16, pp. 67–75, 1997.

[3] Bermes, "Generation and detection of nonlinear lamb waves for the characterization of material nonlinearities," Master's thesis, 2006.

[4] Bermes, C., Kim, J. Y., Qu, J., and Jacobs, L. J., "Experimental characterization of material nonlinearity using lamb waves," *Applied Physics Letters*, vol. 90, 2007.

[5] Blackshire, J. L., Sathish, S., Na, J., and Frouin, J., "Nonlinear laser ultrasonic measurements of localized fatigue damage," *Review of Progress in Quantitative Nondestructive Evaluation*, vol. Volume 657, pp. pp. 1479–1488, 2003.

[6] Buck, O. and Thompson, D. O., "Relation of finite amplitude waves to third order elastic constants," *Materials Science and Engineering*, vol. 1, pp. 117–140, 1966.

[7] Cantrell, J. H., "Substructural organization, dislocation plasticity and harmonic generation in cyclically stressed wavy slip metals," *Proceedings of the Royal Society of London, Series A, Mathematical and Physical Sciences*, p. 757–780, 2004.

[8] Cantrell, J. H. and Yost, W. T., "Nonlinear ultrasonic characterization of fatigue microstructures," *International Journal of Fatigue*, vol. 23, p. 487–490, 2001.

[9] Dace, G. E., Thompson, R. B., Brasche, L. J. H., Rehbein, D. K., and Buck, O., "Nonlinear acoustics, a technique to determine microstructural changes in materials," *Review of progress in quantitative nondestructive evaluation, Plenum Press, New York*, vol. 10B, pp. p. 1685–1692., 1991.

[10] de Lima, W. and Hamilton, M., "Finite-amplitude waves in isotropic elastic plates," *Journal of Sound and Vibration*, vol. 265, p. 819–839, 2003.

[11] Deng, M., "Cumulative second–harmonic generation accompanying nonlinear shear horizontal mode propagation in a solid plate," *Journal of Applied Physics*, vol. 84, p. 3500–3505, 1998.

[12] Deng, M., "Cumulative second–harmonic generation of Lamb–mode propagation in a solid plate," *Journal of Applied Physics*, vol. 85, no. 6, p. 3051–3058, 1999.

[13] Deng, M., "Analysis of second–harmonic generation of Lamb modes using a modal analysis approach," *Journal of Applied Physics*, vol. 94, no. 6, p. 4152–4159, 2003.

[14] Deng, M., "Second–harmonic generation of Lamb modes in a solid layer supported by a semi–infinite substrate," *Journal of Physics D: Applied Physics*, vol. 37, p. 1385–1393, 2004.

[15] Deng, M., Wang, P., and Lv, X., "Experimental observation of cumulative second–harmonic generation of Lamb–wave propagation in an elastic plate," *Journal of Physics D: Applied Physics*, vol. 38, p. 344–353, 2005.

[16] Denga, M. and Pei, J., "Assessment of accumulated fatigue damage in solid plates using nonlinear lamb wave approach," *Applied physics letters*, vol. 90, 2007.

[17] Ginzel, E. A. and Ginzel, R. K., "Ultrasonic Properties of a New Low Attenuation Dry Couplant Elastomer," *Ginzel Brothers & Associates Ltd.*, 1994.

[18] Graff, K. F., *Wave Motion in Elastic Solids*. Dover Publications, first ed., 1975.

[19] Hamilton, M. F. and Blackstock, D. T., *Nonlinear Acoustic*. 1998.

[20] Herrmann, J., *Generation and Detection of Higher Harmonics in Rayleigh Waves Using Laser Ultrasound*. Master's Thesis, School of Civil and Environmental Engineering, Georgia Institute of Technology, 2005.

[21] Herrmann, J., Kim, J. Y., Jacobs, L. J., Qu, J., Littles, J. W., and Savage, M. F., "Assessment of material damage in a nickel–base superalloy using nonlinear Rayleigh surface waves," *Journal of Applied Physics*, vol. 99, no. 12, 2006.

[22] Hikata, A., Chick, B. B., and Elbaum, C., "Dislocation Contribution to the Second Harmonic Generation of Ultrasonic Waves," *Journal of Applied Physics*, vol. 36, no. 1, p. 229–236, 1964.

[23] Hinton, Y. L., Na, J. K., Yos, W. T., and Kessel, G. L., "Field measurement of the acoustic nonlinearity parameter in turbine blades," *NASA Technical Memorandum TM-2000-210303*, 2000.

[24] Huang, K., "On the Atomic Theory of Elasticity," *Proceedings of the Royal Society of London, Series A, Mathematical and Physical Sciences*, vol. 203, no. 1073, p. 178–194, 1950.

[25] Kim, J. Y., Jacobs, L. J., and Qu, J., "Experimental characterization of fatigue damage in a nickel–base superalloy using nonlinear ultrasonic waves," *The Journal of the Acoustical Society of America*, vol. 120, no. 3, 2006.

[26] Nagy, P. B., "Fatigue damage assessment by nonlinear ultrasonic materials characterization," *Ultrasonics*, vol. 36, p. 375–381, 1998.

[27] Niethammer, M., "Application of time frequency representation to characterize ultrasonic signals," Master's thesis, Georgia Institute of Technology, 1999.

[28] Rose, J. L., *Ultrasonic waves in solid media*. Cambridge University Press, 1999.

[29] Shui, Y. and Solodov, I. Y., "Nonlinear properties of Rayleigh and Stoneley waves in solids," *Journal of Applied Physics*, vol. 64, p. 6155–6165, 1988.

[30] Viktorov, I. A., *Rayleigh and Lamb waves: physical theory and applications*. Plenum, New York, 1967.

[31] Weaver, R. L. and Pao, Y.-H., "Spectra of transient waves in elastic plates," *The Journal of the Acoustical Society of America*, vol. 72, p. 1933–1941, 1982.

[32] Yost, W. T. and Cantrell, J. H., "The Effects of Artificial Aging of Aluminum 2024 on its Nonlinearity Parameter," *Review of Progress in Nondestructive Evaluation*, vol. 12, p. 2067–2073, 1993.

[33] Zhou, S. and Shui, Y., "Nonlinear reflection of bulk acoustic waves at an interface," *Journal of Applied Physics*, vol. 72, p. 5070–5080, 1992.